CHALMERS
UNIVERSITY OF TECHNOLOGY

Three-species negative corona discharge simulations using domain decomposition

Master's thesis in Applied Physics

Benjamin Svedung Wettervik

Department of Applied Physics
CHALMERS UNIVERSITY OF TECHNOLOGY
Gothenburg, Sweden 2015

Three-species negative corona discharge simulations using domain decomposition

Benjamin Svedung Wettervik

© Benjamin Svedung Wettervik, 2015.

Department of Applied Physics
Chalmers University of Technology
SE-412 96 Göteborg
Sweden
Tel: +46(0)317721000

Preface

This thesis is partial fulfillment of the requirement for the MSc degree from Chalmers University of Technology. The work was carried out during the period January 2015 to May 2015 at the Fraunhofer Chalmers Centre. Professor Tünde Fülöp at the Department of Applied Phsyics, Division of Nuclear Engineering was examiner and Dr. Tomas Johnson at the Fraunhofer Chalmers Centre was supervisor.

Acknowledgements

This work was supported in part by the Swedish Governmental Agency for Innovation Systems, VINNOVA, through the FFI Sustainable Production Technology program and the project "The virtual Paint Shop e Powder and Externally Charged Wet Paint", and in part by the Sustainable Production Initiative and the Production Area of Advance at Chalmers. The support is gratefully acknowledged.

I would also like to thank the Fraunhofer Chalmers Centre for giving me the opportunity to work on this thesis project. My thanks especially goes to my supervisor Tomas Johnson for our discussions and for his help and guidance throughout this project. I am also grateful to all the people at the Fraunhofer Chalmers Centre that have been a part of and contributed to the project during my time at the centre. Finally, I want to thank my examiner Tünde Fülöp.

Benjamin Svedung Wettervik, Gothenburg, May, 2015

Three-species negative corona discharge simulations using domain decomposition

Benjamin Svedung Wettervik
Department of Applied Physics
Chalmers University of Technology

Abstract

A three-species model for steady-state negative corona discharge has been considered, with focus on geometries occurring in electrostatic precipitators and automotive spray painting. The model incorporates electrons as well as positive and negative ions, which are subject to ionization and attachment reactions. By using the three-species model it is possible to resolve the ionization region, which is not the case in one-species models for corona discharge, although these are commonly used in applications. In this work, we present an approach to solve the three-species problem by decomposing the domain into a one- and three-species part. This is based on that electrons and positive ions exclusively reside in the ionization region, which typically has a small spatial extent. It is an efficient approach as the one-species model is significantly less computationally demanding than the three-species model. The approach is implemented by coupling a structured finite-volume Newton solver for the one-species model and an unstructured finite-volume solver for the three-species model. The implemented solver is validated by considering a one dimensional test case with coaxial cylinders.

The usefulness of the implemented solver is illustrated by solving the three-species problem for a range of geometries of interest to electrostatic precipitators and automotive spray painting. Specifically, we consider electrostatic precipitators with wires that are arranged between parallel plates. The results for these geometries are then used to perform coupled electrostatic-, fluid- and particle-simulations to determine the particle collection efficiency, which is a performance measure for an electrostatic precipitator. Regarding automotive spray painting, we consider two dimensional analogs of the ABB G1 rotary spray bell. We indicate that the results from three-species simulations can be used to parametrize boundary conditions for a one-species solver. This could be a way to efficiently incorporate results from the three-species model in simulations that optimize the spray painting process.

Keywords: negative corona discharge, three-species model, domain decomposition, finite-volume discretization, electrostatic precipitator, automotive spray painting.

Contents

Chapter 1

Introduction

The modeling of ionization phenomena in air plays an important role both in simulations of spray painting in the automotive industry [17] and the analysis of electrostatic precipitators [11, 19, 6, 14, 4]. In the application involving painting, charge that is created by ionization attaches to paint droplets which are guided to the car body by means of an applied voltage. The principle for electrostatic precipitators is similar, although that in this case, the intention is to remove polluting particles from a gas-flow. Reasons to optimize these systems can clearly be connected to the possibility to reduce environmental impact.

In this thesis, we consider models for ionization phenomena that contain either one or three types of charge carriers. These are referred to as single- and three-species models, respectively. Whereas single-species models commonly are used in application-oriented industrial codes, a three-species treatment is necessary to resolve the physical processes that are involved in the ionization. Note that the three-species model is significantly more computationally demanding than the one-species model, which may be one of the reasons for why it is used to a smaller extent.

To present the objective of this thesis, we consider a geometry consisting of sharp objects that are held at a negative potential in relation to some grounded surface. This represents the situation in the previously mentioned applications. For such a configuration it is known that in regions with weak electric fields, the three-species model essentially reduces to a single-species model. This indicates that the three-species problem in the full domain could be solved by using a model that only admits multiple charge carriers locally. Hence, the computational efficiency would be increased as there are more efficient techniques for the one-species problem than for the three-species problem. More precisely, we will in this thesis address the possibility to solve the three-species problem by using domain decomposition and hence split the problem into a globally one-species and locally three-species part.

1.1 Models for ionization phenomena

Here, we give a brief description of the one- and three-species models.

1.1.1 The three-species model

In the three-species model we have three different charge carriers; namely electrons, in combination with a positive ion as well as a negative ion. The three-species model is commonly considered for gases of pure oxygen, and the ions can in that case be represented by O_2^+ and O_2^- [22, 8, 23, 3, 28, 25, 1, 27, 10]. In air, one may instead consider the positive and negative ions as average representations of a slightly wider range of species. These charge carriers are associated with charge densities ρ_e, ρ_p and ρ_n, which satisfy the transport equations:

$$\nabla \cdot (\mu_e \rho_e \nabla \phi) = k_i \rho_e - k_a \rho_e,$$

$$\nabla \cdot (\mu_p \rho_p \nabla \phi) = k_i \rho_e,$$

and

$$\nabla \cdot (\mu_n \rho_n \nabla \phi) = k_a \rho_e,$$

where ϕ is the electrostatic potential. In these equations, k_i and k_a are reaction rates, and μ_e, μ_p, and μ_n are mobilities, which depend on the electric field. Keeping the positive and negative oxygen ions as notation for the ions in our model, the reaction rates correspond to the ionization reaction:

$$e + O_2 \to 2e + O_2^+,$$

and the attachment reaction:

$$e + O_2 + M \to O_2^- + M,$$

where M is an uncharged species. In addition to these equations, ϕ should satisfy the Poisson equation:

$$-\Delta\phi = \frac{1}{\epsilon_0}(\rho_e + \rho_p + \rho_n).$$

Regarding boundary conditions, we note that a typical geometry consists of a sharp object Γ_E and some surface Γ_0, between which one applies a negative potential difference. Using this notation; there are five boundary conditions:

$$\phi = 0 \quad \text{on} \quad \Gamma_0,$$

$$\phi = -V_E \quad \text{on} \quad \Gamma_E,$$

$$\rho_n = 0 \quad \text{on} \quad \Gamma_E,$$

$$\rho_p = 0 \quad \text{on} \quad \Gamma_0,$$

$$0 = \gamma \mu_p \rho_p + \mu_e \rho_e \quad \text{on} \quad \Gamma_E,$$

where γ is the second Townsend Ionization Coefficient.

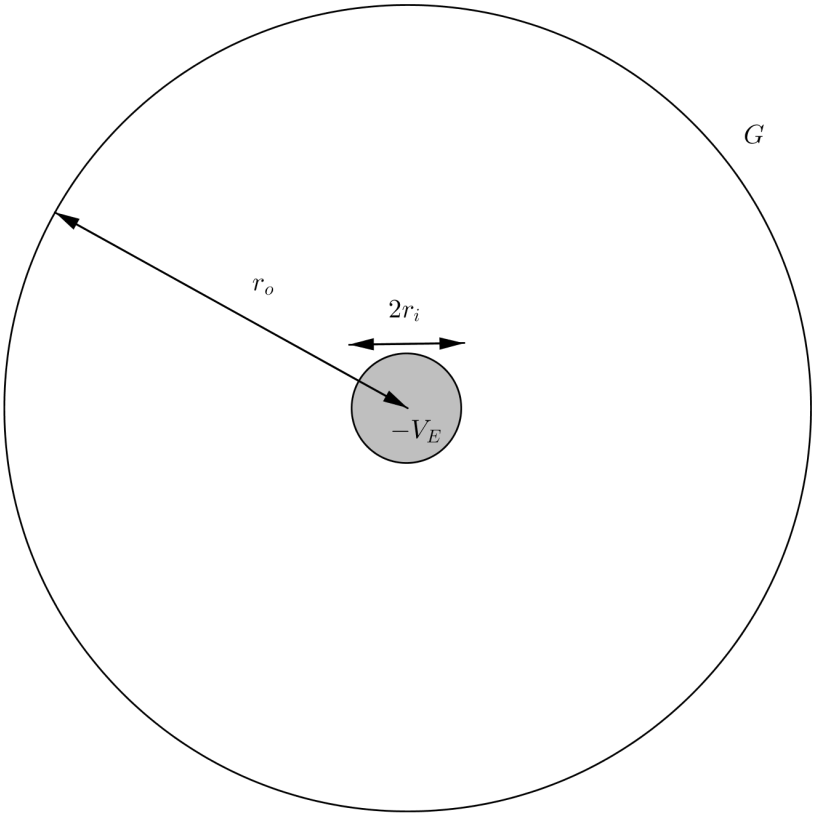

Figure 1.1: Geometry with coaxial cylinders, i.e. an inner cylinder with radius r_i which is surrounded by an outer cylindrical shell, with radius r_o. The inner cylinder is held at a negative potential, $-V_E$, compared to the outer cylindrical shell, which is grounded.

1.1.2 The one-species model

In the three-species model, positive ions and electrons exclusively reside in a small region, referred to as the corona or ionization region, in the close vicinity of Γ_E. To illustrate this, we consider a geometry with coaxial cylinders, where the inner cylinder has radius $r_i = 1.35\,\mathrm{mm}$, the outer cylinder has radius $r_o = 5\,\mathrm{cm}$ and the applied voltage corresponds to $V_E = 26\,\mathrm{kV}$. This configuration is schematically illustrated in Figure 1.1. The charge densities for electrons as well as positive and negative ions are shown in Figure 1.2. Based on this, we see that the dimensions of the region where more than one charge carrier is present only extends a few millimeters from the inner cylinder. Outside this region, the reaction terms vanish and the system can to a high degree of accuracy be described by:

$$\nabla \cdot (\mu\rho\nabla\phi) = 0 \quad \text{and} \quad -\Delta\phi = \rho/\epsilon_0,$$

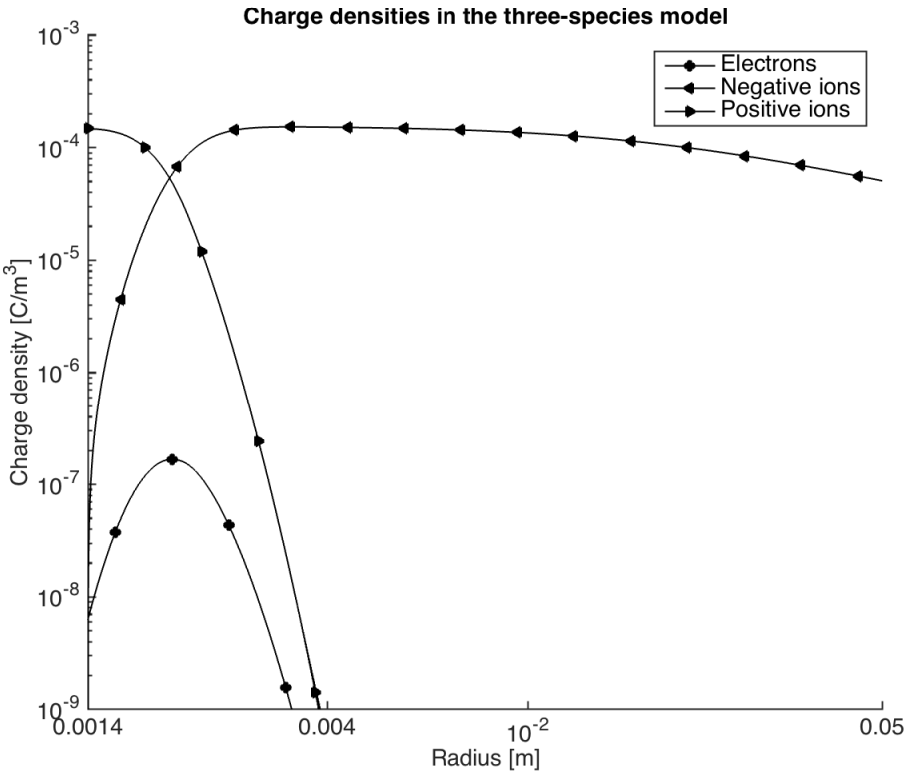

Figure 1.2: Absolute values of charge densities for electrons as well as positive and negative oxygen ions, as a function of the radial distance, in a geometry with coaxial cylinders. The radius of the inner cylinder is $r_i = 1.35\,\mathrm{mm}$ and the radius of the outer cylinder is $r_o = 5\,\mathrm{cm}$. The applied voltage is $V_E = 26\,\mathrm{kV}$.

where ρ denotes the total charge density, which is dominated by the contribution from negative ions. This is a one-species model and needs a boundary condition for the negative ion charge density at Γ_E, which is non-trivial to obtain. Hence, in models that are based solely on a one-species description one must make use of empirical criteria [2, 7, 18] to obtain boundary conditions. For example, such boundary condition can be based on the Kaptzov hypothesis, which states that the electric field at Γ_E is equal to the threshold field-strength for corona discharge. This is a common approach in industrial solvers. Unfortunately, it is neither a numerically nor mathematically stable approach.

1.1.3 A note on reaction rate-, mobility- and secondary emission-coefficients

As shown in [8], the coefficients that are used for reaction rates and mobility constants vary significantly between different studies. Experimental data for reaction rates an mobility constants has e.g. been gathered by Eliasson and Kogelschatz [5], and Raju [24]. For the calculations in this thesis, we have primarily used the data that was gathered by Eliasson and Kogelschatz. Also, we have considered coefficients for pure oxygen, as this yields slightly better stability properties than if the coefficients for air are used. The coefficients are functions of E/N, where E is the electric field strength and N is the number density for neutral particles. Recall that $N = 2.46 \cdot 10^{25}\,\mathrm{m}^{-3}$ at normal temperature and pressure. Here, E/N is expressed in the unit Townsend [Td], for which $1\,\mathrm{Td} = 10^{-21}\,\mathrm{Vm}^2$. Spline approximations of the reaction rate and electron mobility coefficients are shown in Figure 1.3. Regarding the ion mobilities, we use $\mu_p = \mu_n = 2.0 \cdot 10^{-4}\,\mathrm{m}^2/\mathrm{Vs}$. Finally, the secondary emission coefficient is taken to $\gamma = 0.01$.

1.2 Numerical challenges with the one- and three-species models

The main challenge in solving the equations for either the one-species or three-species model lies in the treatment of the nonlinearities of the equations. For both problems, there is a nonlinear coupling between the charge-densities and the electric field. For the three-species model, the reaction terms also have a strong dependence on the electric field and vary several orders of magnitude in a small part of the domain. To find the steady-state solution, an initial approximation of the solution is chosen, and then used to generate a sequence of linear problems, e.g. by means of Picard iteration or Newtons method. The approximation is updated until it has converged within some reasonable level of accuracy. Here, it should be noted that the use of Newtons method yields better convergence properties, which makes it preferable, provided that the resulting linear problems are feasible.

For the one-species problem, the Newtons method results in linear problems that can be solved by means of iterative linear solvers; as is necessary for large scale simulations. For the three-species model, on the other hand, the sparsity pattern of the Jacobian matrix is more problematic. Since the problem is reaction dominated in parts of the domain; the coupling between the electron charge density and the remaining charge densities causes large off-diagonal terms. As stated by the Scarborough criterion, iterative linear solvers are guaranteed to converge if the matrix is diagonally dominant; but may otherwise fail. On the practical level; the options are to modify the Jacobian, tailor efficient preconditioning schemes, or use non-iterative linear solvers, e.g LU-solvers. The first option comes at the price of slower convergence with respect to the number of iterations and the third option is only viable for smaller systems due to the scaling of the computational cost. Preconditioning might be viable but there is a sharper threshold to obtain a working solution. By using a domain decomposition approach, on the

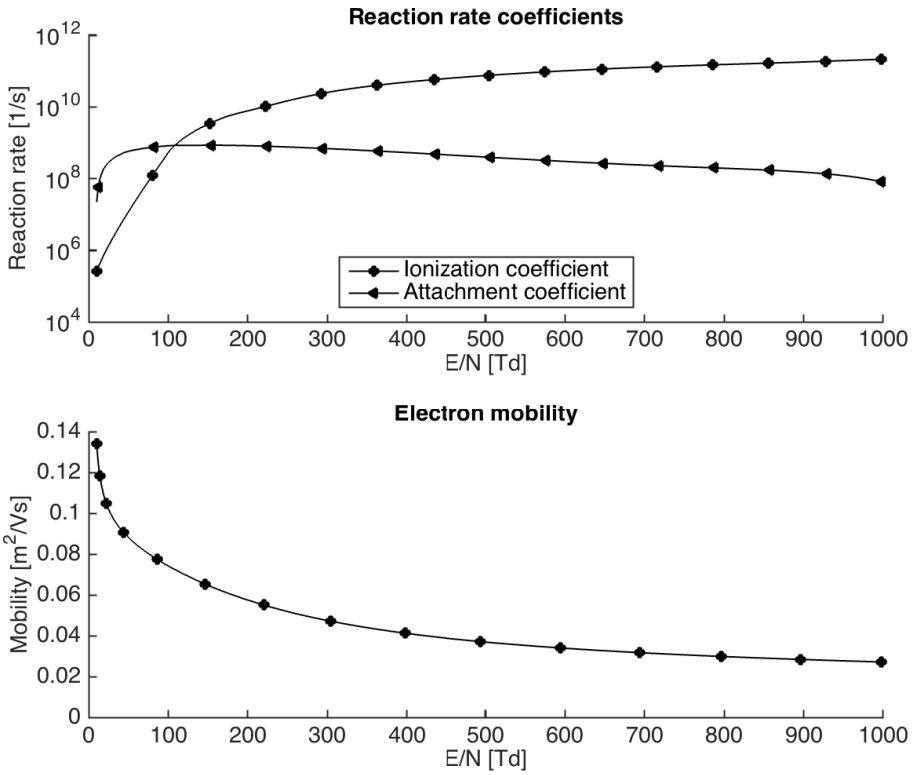

Figure 1.3: Coefficients for reaction rates, k_i and k_a, as well as the electron mobility μ_e, according to experimental data collected by Eliasson and Kogelschatz [5]. Here, we use the unit Townsend [Td] for E/N, where E is the electric field strength and N is the number density of neutral particles.

other hand, it is still possible to use the third option for the local solvers at the same time as the problems associated with the scaling of the computational cost are avoided.

1.3 Outline

This thesis is divided into five primary parts, describing numerical schemes, their implementations, and finally a selected number of applications. The first part, in Chapter 2 describes a finite-volume discretization for a structured single-species Newton solver in three dimensions. This is an existing code in the in-house multi-physics solver IBOFlow [16, 15], which has been developed at the Fraunhofer Chalmers Centre. We also describe the implementation of a two dimensional unstructured finite-volume solver for the three-species model. This is an extension

of a two dimensional solver that uses cylindrical coordinates ((r,z)-coordinates) [10]. This is followed by Chapter 3, which treats the coupling between three-species solvers and the global Newton solver. We describe the treatment of boundary conditions, interpolations between different meshes, and modifications of the Newtons method. Then, in Chapter 4, we validate the implemented solvers and make performance evaluations. Finally, two Chapters are devoted to applications. In Chapter 5, we analyze the three-species problem for geometries of interest to electrostatic precipitators, as well as some multipole geometries, which are relevant to automotive spray painting. Regarding Chapter 6, we make a more in depth detour into the application with electrostatic precipitators. We couple the solutions that were obtained in Chapter 5 to a fluid solver and trace trajectories of particles; leading to predictions of collection efficiencies for electrostatic precipitators.

Chapter 2

Finite volume solvers for the one- and three-species model

In this chapter, we present the one- and three-species solvers that will be used as global and local solvers, respectively, in the implementation of domain decomposition for the three-species problem. As a global solver, we will use the three dimensional structured finite volume Newton solver that was mentioned in the introductory outline in Section 1.3. Here, we will present its discretization, and discuss the mesh structure as well as the implementation of boundary conditions, which is of interest to the presentation in Chapter 3. Regarding local solvers, we will describe the implementation of a two dimensional unstructured finite volume solver in cartesian coordinates. This solver is an extension of a similar solver in cylindrical (r,z)-coordinates [10] and has been developed in this work. We will present its discretization and discuss the modifications that were necessary due to complications because of the transition to cartesian coordinates.

2.1 A structured finite volume solver using Newtons method for the one-species model

Here, we introduce concepts related to the discretization of a structured finite volume Newton solver for the one-species model.

2.1.1 Definition of mesh structure and discretized quantities

The discretization for the Newton solver utilizes an octree mesh, as is implemented in the in-house multi-physics code IBOFlow, at the Fraunhofer Chalmers Centre [16, 15]. A two dimensional illustration, i.e. a quad-tree counterpart, of such mesh is given in Figure 2.1. In the octree mesh, space is partitioned into cells which may be refined by subdivision into eight smaller cells. This can be described as a tree-structure, where the level of a leaf is defined by

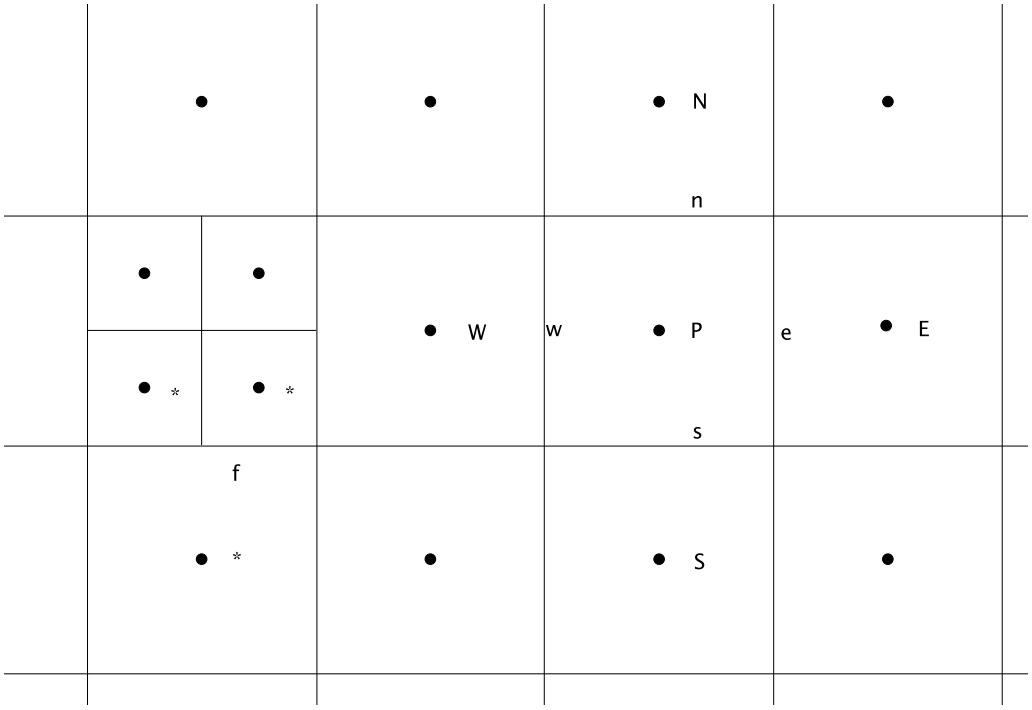

Figure 2.1: Two dimensional illustration of a structured grid, which introduces notation for a cell P and its neighbors E, W, N and S as well as the corresponding faces e, w, n and s. Adjacent cells may vary by one level of refinement, such as the cells that share the face denoted by f. When interpolating face values for non-matching faces, a stencil containing the points marked by $(*)$ is used.

the number of refinements that were used upon its creation. By subdividing different cells a different number of times, it is possible to obtain a mesh with varying resolution in different parts of the domain.

To discretize various quantities, we use cell-centered values. The value corresponding to a generic cell is denoted by ϕ_P for the potential and by ρ_P for the charge density. In the finite volume method, we need to interpolate face values and gradients. This is performed by using cell-centered values from adjacent cells. As is indicated in Figure 2.1, the adjacent cells associated with a cell P are denoted by E (east), W (west), N (north), S (south), T (top, not shown), and B (bottom, not shown). Furthermore, the faces that are shared with these cells are denoted by e, w, n, s, t, and b, respectively.

In the discussion of discretizations, we need to consider the possibility that adjacent cells have different size. More exactly, a pair of adjacent cells are allowed to differ in refinement level by one subdivision, which admits for the existence of non-matching faces. This is exemplified in Figure 2.1. To express face values and gradients on a non-matching face f, a wider stencil

must be used compared to if the faces match. In the figure, the cell-centered values that are used to interpolate the face value are marked by $(*)$. With this pointed out, we may continue the presentation with the assumption that adjacent faces are matching, and note that the principles for the non-matching case are similar, although the stencil is slightly different.

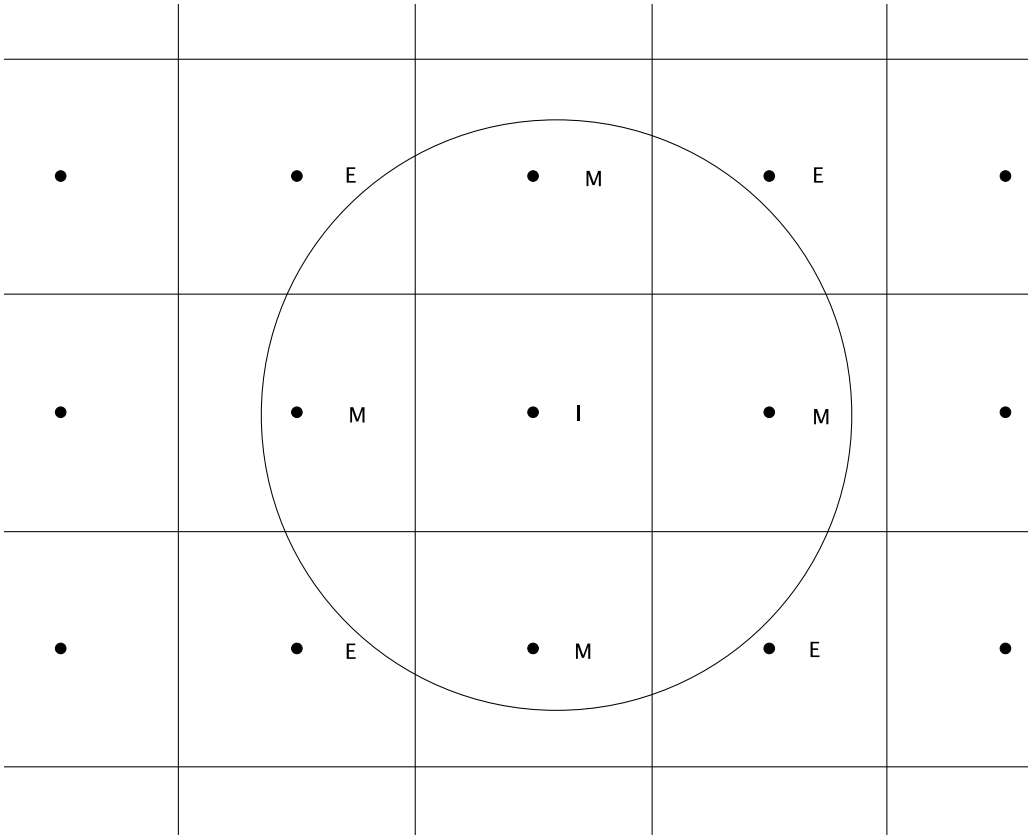

Figure 2.2: Two dimensional illustration of a structured grid with a circular immersed boundary. The cells that either are inside or have centers that are less than half the cell size away from the immersed boundary are labeled interior- (I), mirroring- (M) and extrapolation cells (E), respectively.

2.1.2 Immersed boundary conditions

The boundary conditions on geometric structures in the domain are implemented by using the mirroring immersed boundary method [16, 15]. To describe this method, which is second order accurate, we consider a circular boundary as is shown in Figure 2.2. Assume that this boundary is associated with a Dirichlet boundary condition Φ_{bc} for a quantity Φ (either the potential or the charge density), that is defined on the cell-centers. According to the mirroring immersed

boundary method, cells that either are inside or have centers that are less than half the cell size away from the immersed boundary are labeled as interior-, mirroring- or extrapolation cells. Interior cells lie inside the immersed boundary, with cell-centers that have a larger distance to the immersed boundary than one and a half cell size. The remaining cells that fit the above description are labeled as mirroring cells or extrapolation cells, depending on if their cell-center lies inside or outside the immersed boundary.

The equation for an interior point is implemented as a diagonal element with the right hand side equal to Φ_{bc}. For mirroring cells one defines a point by mirroring the cell center in the boundary, along the normal. Denoting the value at the cell-center of the mirroring cell by Φ_P and the value at the mirrored point by Φ_{mirror}, it should hold that:

$$\Phi_{\text{bc}} = \frac{\Phi_P + \Phi_{\text{mirror}}}{2}. \tag{2.1}$$

Clearly, Φ_{mirror} does not in general correspond to a value at a cell-center, but can be expressed in terms of cell-centered quantities by using trilinear interpolation. Regarding extrapolation cells, the closest point on the immersed boundary is mirrored in the cell-center of the extrapolation cell. If Φ_P denotes the value at the cell-center of the extrapolation cell and $\Phi_{\text{extrapolation}}$ is the value at the point that has been extrapolated by mirroring, it should hold that:

$$\Phi_P = \frac{\Phi_{\text{bc}} + \Phi_{\text{extrapolation}}}{2}, \tag{2.2}$$

where $\Phi_{\text{extrapolation}}$ is expressed by interpolation of cell-centered quantities.

In addition to Dirichlet boundary conditions, we may also have Neumann conditions. At a cell that is inside the domain, but with a face at the boundary, this yields a relation between the cell-centered value and the value at the mirror point of the cell-center through the boundary. This can then be used to express the face value at the boundary solely in terms of quantities inside the domain.

2.1.3 Finite volume discretization of Newtons method for the single-species model

Let (ϕ,ρ) be an approximation to the solution in the one-species model and assume that ($\delta\phi$,$\delta\rho$) is such that ($\phi + \delta\phi$,$\rho + \delta\rho$) solves the equations. By integrating both sides of the equation for the potential over the volume of the cell P, we get:

$$-\int_V \Delta(\phi + \delta\phi)\,\mathrm{d}V = \int_V \frac{1}{\epsilon_0}(\rho + \delta\rho)\,\mathrm{d}V, \tag{2.3}$$

which by using Gauß theorem can be written as:

$$-\int_{\partial V} \nabla(\phi + \delta\phi)\cdot \mathrm{d}S = \int_V \frac{1}{\epsilon_0}(\rho + \delta\rho)\,\mathrm{d}V. \tag{2.4}$$

Hence, we obtain that:

$$-\int_{\partial V} \nabla\delta\phi \cdot \mathrm{d}S - \int_V \frac{1}{\epsilon_0}\delta\rho \,\mathrm{d}V = \int_{\partial V} \nabla\phi \cdot \mathrm{d}S + \int_V \frac{1}{\epsilon_0}\rho \,\mathrm{d}V. \tag{2.5}$$

The flux integrals involving $\nabla\phi$ are evaluated by using a central difference approximation for $\nabla\phi \cdot n$ which is multiplied by the area of the face, where n denotes the outward normal. The volume integral with respect to the charge density is evaluated by multiplying the cell-centered value by the volume of the cell. If we, for notational simplicity, assume that the mesh is isotropic with cubic cells of side length L, we obtain:

$$\begin{aligned}(6\delta\phi_P - \delta\phi_E - \delta\phi_W - \delta\phi_N - \delta\phi_S - \delta\phi_T - \delta\phi_B) - L^2\frac{1}{\epsilon_0}\delta\rho_P = \\ (\phi_E + \phi_W + \phi_N + \phi_S + \phi_T + \phi_B - 6\phi_P) + L^2\frac{1}{\epsilon_0}\rho_P,\end{aligned}$$

after dividing by all common factors of L, which defines a system of linear equations.

In addition to the Poisson equation, we have the transport equation for ρ, which takes the form:

$$0 = \int_V \nabla \cdot (\mu(\rho + \delta\rho)\nabla(\phi + \delta\phi)) \,\mathrm{d}V = \int_{\partial V} \mu(\rho + \delta\rho)\nabla(\phi + \delta\phi) \cdot \mathrm{d}S, \tag{2.6}$$

where the last step follows from Gauß theorem. By rearranging this, we obtain that:

$$\int_{\partial V} \mu\delta\rho\nabla\phi \cdot \mathrm{d}S + \int_{\partial V} \mu\rho\nabla\delta\phi \cdot \mathrm{d}S = -\int_{\partial V} \mu\rho\nabla\phi \cdot \mathrm{d}S, \tag{2.7}$$

provided that we only keep terms up to linear order in ($\delta\phi$,$\delta\rho$). Here, expressions involving the gradient of the potential and its correction are evaluated in the same way as in the discussion of the Poisson equation, which results in a discretization of the form:

$$\begin{aligned}\delta\rho_e(\phi_E - \phi_P) + \delta\rho_w(\phi_W - \phi_P) + \delta\rho_n(\phi_N - \phi_P) + \delta\rho_s(\phi_S - \phi_P) + \\ \delta\rho_t(\phi_T - \phi_P) + \delta\rho_b(\phi_B - \phi_P) + \rho_e(\delta\phi_E - \delta\phi_P) + \rho_w(\delta\phi_W - \delta\phi_P) + \\ \rho_n(\delta\phi_N - \delta\phi_P) + \rho_s(\delta\phi_S - \delta\phi_P) + \rho_t(\delta\phi_T - \delta\phi_P) + \rho_b(\delta\phi_B - \delta\phi_P) = \\ -\rho_e(\phi_E - \phi_P) - \rho_w(\phi_W - \phi_P) - \rho_n(\phi_N - \phi_P) - \rho_s(\phi_S - \phi_P) - \\ \rho_t(\phi_T - \phi_P) - \rho_b(\phi_B - \phi_P),\end{aligned}$$

where we have divided by all common factors of L and μ. The remaining part is to express the face values of ρ and $\delta\rho$ in terms of cell-centered quantities. Here, the interpolation will be performed using the Normalized Variable Diagram, which is described in Section 2.1.4.

2.1.4 Interpolation of face values for ρ by using the Normalized Variable Diagram

The face value for the charge density corresponding to an arbitrary face f will be denoted by ρ_f. We will use the Normalized Variable Diagram to express the face value in terms of a stencil

consisting of three points. This formalism includes a wide range of interpolation schemes with different orders of accuracy [12, 13]. Generally it can be stated that a well designed interpolation scheme should be conservative, monotonous, and yield matrices that are diagonally dominant. As the equations under consideration may have solutions that exhibit steep gradients, the use of higher order schemes demands the use of limiters to meet these standards.

To define the Normalized Variable Diagram we label the cells that share f as donor cell D and acceptor cell A, where the labeling is determined by the flow direction at f. In addition to this, we have the upwind U cell, which is the cell that is on the opposite side of the donor cell as compared to the acceptor cell. With these cells defined, normalized coordinates are introduced according to:

$$\tilde{\rho} = \frac{\rho - \rho_U}{\rho_A - \rho_U}. \tag{2.8}$$

Note that $\tilde{\rho}_U = 0$ and that $\tilde{\rho}_A = 1$. Now, using the normalized coordinates, $\tilde{\rho}_f$ can be expressed as a function of $\tilde{\rho}_D$, which defines an interpolation scheme. With the calculated value for $\tilde{\rho}_f$, one may evaluate:

$$\beta = \frac{\tilde{\rho}_f - \tilde{\rho}_D}{\tilde{\rho}_A - \tilde{\rho}_D}, \tag{2.9}$$

which can be rewritten as:

$$\rho_f = (1 - \beta)\rho_D + \beta\rho_A. \tag{2.10}$$

Hence, the dependence on the upwind cell has been absorbed into the coefficient β, which is calculated explicitly. Note that it must hold that $\beta \in [0,1]$, or the interpolation may fail to be monotonous and the solution will exhibit oscillations. It is hence necessary to enforce that $\tilde{\rho}_D \leq \tilde{\rho}_f \leq 1$. Regarding interpolation schemes, we have the first order upwind scheme, for which $\tilde{\rho}_f = \tilde{\rho}_D$. Among higher order schemes, we have second order upwinding ($\tilde{\rho}_f = 3\tilde{\rho}_D/2$), Fromm's method ($\tilde{\rho}_f = 1/4 + \tilde{\rho}_D$) and the QUICKEST-scheme ($\tilde{\rho}_f = 3/8 + 3\tilde{\rho}_D/4$).

2.2 Two dimensional unstructured finite volume solver for the three species model

Here, we introduce concepts related to the discretization of an unstructured finite volume solver in cartesian coordinates, for the three species model. In contrast to the solution procedure that was presented for the one-species problem in Section 2.1, we will make an uncoupled treatment of the Poisson equation and charge densities. This means that we may describe the discretization for the Poisson equation and charge densities separately as is done in Sections 2.2.3 and 2.2.4.

2.2.1 Definition of mesh structure and discretized quantities

The unstructured solver uses a two dimensional mesh with triangular elements, as is illustrated in Figure 2.3. Solution quantities are defined on the centers of the triangles, which are referred

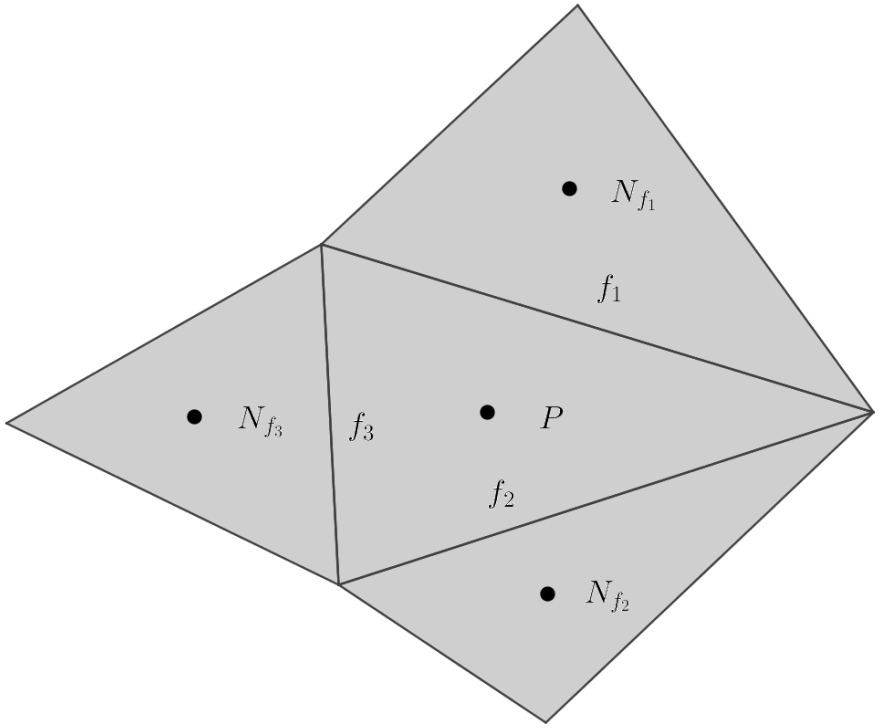

Figure 2.3: Showing triangles that introduce notation for an unstructured mesh. The edges for the triangle P are denoted by f_i, where $i = 1$, 2 or 3. Furthermore, the triangle sharing the edge f_i is denoted by N_{f_i}.

to as cell-centers. For a triangle, labeled P, we denote its edges by f and the adjacent triangle sharing a given edge f by N_f. Furthermore, $|f|$ denotes the length of the edge f and $|T|$ denotes the area of the triangle T.

2.2.2 Interpolation to edges

In the finite volume scheme for the three-species model on an unstructured mesh, the electric field, the mobility constants as well as the charge densities, will need to be evaluated at the

edges of the triangles. This is slightly more complicated than in the structured case as the cell-centers of adjacent triangles have a more arbitrary relation to the location and orientation of a shared edge. To accommodate this, we use linear interpolation of the form:

$$\Phi_f = (1 - I_f)\Phi_P + I_f\Phi_{N_f}, \tag{2.11}$$

with an interpolation coefficient I_f that is given by:

$$I_f = \frac{d(P,f)}{d(P,f) + d(N_f,f)}. \tag{2.12}$$

Here, Φ is a cell-centered quantity and $d(\cdot,\cdot)$ denotes the shortest distance between a cell-center and an edge.

For edge values of gradient vectors, the same interpolation is used, provided that the gradients have been evaluated at the cell-centers. To evaluate cell-centered gradients, we use Greens formula:

$$\int_{\partial T} f\,\mathrm{d}y - g\,\mathrm{d}x = \int_T \left(\frac{\partial f}{\partial x} + \frac{\partial g}{\partial y}\right)\mathrm{d}x\mathrm{d}y. \tag{2.13}$$

Hence, the cell-centered gradient of Φ, can be expressed as:

$$\nabla\Phi_f = \frac{1}{|T|}\begin{pmatrix} \Phi_{f_1}\Delta y_1 + \Phi_{f_2}\Delta y_2 + \Phi_{f_3}\Delta y_3 \\ -\Phi_{f_1}\Delta x_1 - \Phi_{f_2}\Delta x_2 - \Phi_{f_3}\Delta x_3 \end{pmatrix}, \tag{2.14}$$

which makes use of the edge values of Φ. Here Δx_i and Δy_i are the changes in the coordinates when traversing between the endpoints of an edge in a counter-clockwise direction. Finally, note that this formula also has applications when defining edge-values at boundaries with Neumann boundary conditions for Φ.

2.2.3 Discretization for the Poisson equation

To discretize the Poisson equation, we integrate the equation over a triangle T:

$$-\int_T \Delta\phi\,\mathrm{d}V = \int_T \frac{1}{\epsilon_0}\rho\,\mathrm{d}V. \tag{2.15}$$

By using the divergence theorem and approximating the involved integrals using discretized quantities, we obtain that:

$$-\sum_f \nabla\phi_f \cdot n_f|f| = \frac{1}{\epsilon_0}\rho_P|T|. \tag{2.16}$$

Here, it is the evaluation of $\nabla\phi_f \cdot n_f$, which poses the largest challenge. This occurs since the line passing through the cell-centers of adjacent triangles is not necessarily collinear with the

normal n_f of the shared edge. Because of this, $\nabla\phi_f \cdot n_f$ is split into an implicit and explicit part, and the potential is found by an iterative procedure. More exactly, $\nabla\phi_f \cdot n_f$ is decomposed as:

$$\nabla\phi_f \cdot n_f = \frac{|D_f|}{|d_f|}(\phi_{N_f} - \phi_P) + R_f \cdot \nabla\phi_f \tag{2.17}$$

where d_f is the vector from P to N_f. Furthermore, the terms D_f and R_f are defined as:

$$D_f = \frac{|f|d_f}{d_f \cdot n_f} \quad \text{and} \quad R_f = |f|n_f - D_f. \tag{2.18}$$

In this representation, the term involving D_f is treated implicitly, and R_f is treated explicitly. To evaluate R_f, the gradient of the potential from the previous iteration is evaluated on the edge, as was described in Section 2.2.2.

To summarize, the Poisson equation is discretized according to:

$$-\sum_f \frac{|D_f|}{|d_f|}(\phi_{N_f} - \phi_P) = \sum_f R_f \cdot \nabla\phi_f + \frac{1}{\epsilon_0}\rho_P|T| \tag{2.19}$$

where implicit terms are on the left hand side and explicit terms are on the right hand side.

Regarding boundary conditions, Dirichlet boundary conditions are implemented by modifying the evaluation of $\nabla\phi_f \cdot n_f$ at the edges f that correspond to a Dirichlet boundary. In that case, the potential has a prescribed value ϕ_{bc} on the edge and $\nabla\phi_f \cdot n_f$ is given by:

$$\nabla\phi_f \cdot n_f = \frac{\phi_{\text{bc}} - \phi_P}{d(P,f)}. \tag{2.20}$$

In addition to this, homogenous Neumann boundary are implemented by imposing that $\nabla\phi_f \cdot n_f = 0$ in (2.16).

2.2.4 Discretization of a transport equations

In this section, we discuss the discretization of the transport equations for electrons as well as positive ions and negative ions. Observe that the transport equations for the charge densities can be written on the generic form:

$$\nabla \cdot (\mu_i \nabla\phi\rho_i) = S_i(E)\rho_e, \tag{2.21}$$

where i is an index for the charge density and μ_i, $S_i(E)$ is the corresponding mobility and reaction rate coefficient. Depending on which species that is considered, we may either have that $S_i(E)$ equals k_i, $(k_i - k_a)$ or k_a.

In the discretization, we will solve for updates ($\delta\rho_e$,$\delta\rho_n$,$\delta\rho_p$) of the current approximation of the solution (ρ_e,ρ_n,ρ_p). In this notation; integration of a transport equation over a triangle T and application of the divergence theorem yields:

$$\int_{\partial T} \mu_i \delta\rho_i \nabla\phi \cdot \mathrm{d}S - \int_T S_i(E)\delta\rho_e \,\mathrm{d}V = \\ -\int_{\partial T} \mu_i \rho_i \nabla\phi \cdot \mathrm{d}S + \int_T S_i(E)\rho_e \,\mathrm{d}V,$$

after rearranging the terms so that the terms in the left hand side are treated implicitly and the terms in the right hand are treated explicitly. The discretized version of the above equation is given by:

$$\sum_f \mu_{if}\delta\rho_{if}\nabla\phi_f \cdot n_f|f| - S_i(E)\delta\rho_{eP}|T| = \\ -\sum_f \mu_{if}\rho_{if}\nabla\phi_f \cdot n_f|f| + S_i(E)\rho_{eP}|T|.$$

In this expression, the edge values of the charge densities are expressed using the Normalized Variable Diagram and gradients are interpolated according to Section 2.2.2. Regarding values for reaction rates, these are first interpolated to the edges and then back to the cell-centers. This serves to increase stability by widening the stencil and hence compensate for inaccuracies that may appear in the calculation of the electric field in a single cell.

As was mentioned in the introduction to this thesis, the coupling of the charge densities through the reaction term yields a sparsity pattern with large off-diagonal elements. Hence, one may argue that it is favorable to drop the coupling between the charge densities and make a fully uncoupled treatment of the problem. This works in cylindrical coordinates as is shown in [10]. In cartesian coordinates, however, an uncoupled treatment was experienced to lead to instability for the test case in Chapter 4. Hence, the three-species solver in cartesian coordinates will generally demand the use of non-iterative linear solvers. Additionally, in order to favor stability a relaxation parameter ω is introduced and the equations are modified according to:

$$\sum_f \mu_{if}\delta\rho_{if}\nabla\phi_f \cdot n_f|f| - \omega S_i(E)\delta\rho_{eP}|T| = \\ -\sum_f \mu_{if}\rho_{if}\nabla\phi_f \cdot n_f|f| + S_i(E)\rho_{eP}|T|.$$

This is motivated by the fact that the reaction rates have a strong dependence on the electric field strength, which typically is known to rather low accuracy during the initial part of the solution process. To see that this modification is admissible it should be noted that the correct solution to the transport equations corresponds to that the right hand side becomes zero, and as long as this can be ensured, it does not matter if the matrix that is defined by the left hand side is altered. Typically, we take $\omega \in [0.1, 1]$, depending on the problem at hand.

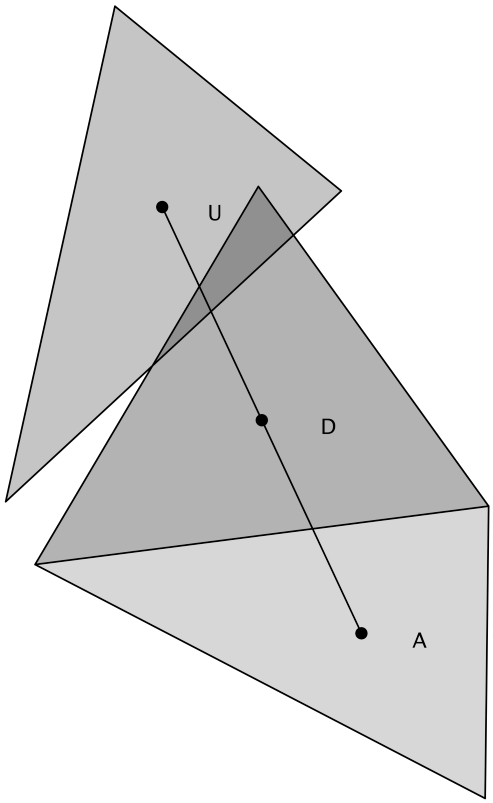

Figure 2.4: Showing the ghost upwind triangle (labelled U) which is obtained by reflecting the acceptor triangle (A) in the cell-center of the donor triangle (D) along the line connecting the cell-centers of the acceptor and donor triangle.

2.2.5 Interpolation of face values for ρ_i and the unstructured solver

As stated in the previous section, the Normalized Variable Diagram is used to interpolate edge values for the charge densities. For an unstructured mesh, the acceptor and donor cell can be defined similarly as in the structured case. For the upwind cell, on the other hand, it is more difficult to make a definition based on a neighboring triangle. This is avoided by introducing a ghost-triangle, as is shown in Figure 2.4. The ghost triangle is constructed by mirroring the acceptor triangle in the cell-center of the donor triangle, along the line that connects the acceptor and donor cell-centers.

It is necessary to interpolate the value of the charge density to the cell-center of the ghost-triangle. This is performed by using a central-differencing approach, based on the gradient in the donor cell:

$$\nabla \rho_{iD} \cdot \hat{d}_f = \frac{\rho_{iA} - \rho_{iU}}{2|d_f|}, \tag{2.22}$$

where $\hat{d}_f$ is a unit-vector in the direction of d_f. By using the value of ρ_{iU}, it is possible to define $\tilde{\rho}_{iA}$, $\tilde{\rho}_{iU}$, $\tilde{\rho}_{iD}$ and $\tilde{\rho}_{if}$ in the same way as for the structured case. On the other hand, as the value in the upwind triangle is interpolated, to favor stability, an artificial Courant number c is introduced and $\tilde{\rho}_{if}$ is transformed according to:

$$\tilde{\rho}_{if} \to (1-c)\tilde{\rho}_{if} + c\tilde{\rho}_{iD}. \tag{2.23}$$

The value of $\tilde{\rho}_{if}$ is then limited according to $\tilde{\rho}_{iD} \leq \tilde{\rho}_{if} \leq 1$ and $\tilde{\rho}_{if} \leq \tilde{\rho}_{iD}/c$, and finally used to define β as in the structured case.

2.3 Convergence criteria

As the solution process is iterative, it is necessary to have a termination criterion for when a solution of sufficient accuracy has been found. Here, we will use the total relative update Δ_{l^2} in l^2 norm, which for the Newton solver can be defined as:

$$\Delta_{l^2}^2 = \frac{||\Delta\rho||_{l^2}^2}{||\rho||_{l^2}^2} + \frac{||\Delta\phi||_{l^2}^2}{||\phi||_{l^2}^2} \tag{2.24}$$

and as:

$$\Delta_{l^2}^2 = \frac{||\Delta\rho_p||_{l^2}^2}{||\rho_p||_{l^2}^2} + \frac{||\Delta\rho_e||_{l^2}^2}{||\rho_e||_{l^2}^2} + \frac{||\Delta\rho_n||_{l^2}^2}{||\rho_n||_{l^2}^2}, \tag{2.25}$$

for the three-species solver. Here, a Δ proceeding a solution quantity refers to the difference in the solution between consecutive iterations.

Chapter 3

A domain decomposition approach

This chapter presents a domain decomposition approach to the three-species problem. To give an overview of the approach, we consider the geometry with a pair of coaxial cylinders that is shown in Figure 3.1, for which the inner cylinder is held at a lower potential compared to the outer cylinder. This divides space into an ionization region and a region where the one-species model is valid. Similarly, we will in our approach apply a three-species solver to a domain that is slightly larger than the ionization region. The goal is to use the local three-species solver to set boundary conditions for the charge density in a single-species solver that operates in the full domain so that the one-species solution assumes the same behavior as the three-species solution, outside the ionization region.

We will consider two different approaches to set the boundary condition for the charge-density for the single-species solver. The first approach is to use the three-species solution to solve the one-species problem to the physical boundary of the domain and set a boundary condition there. The second approach is to introduce an artificial boundary that surrounds the ionization region on which the charge density from the three-species solver is used as a boundary condition. The former approach has the benefit that the boundary condition for the single-species charge density and potential can be set on the same boundary. On the other hand, corona-phenomena are highly directional in complicated geometries. Hence, setting a boundary condition for the charge density at the physical boundary demands that the mesh for the one-species solver can resolve this directionality at the length-scale of this boundary. This favors the use of an artificial boundary inside the domain as it admits for the use of a coarser mesh in the single-species solver.

3.1 The coupling of global and local solvers

With the notation that was introduced in Figure 3.1, we intend to solve the equations:

$$\nabla \cdot (\mu\rho\nabla\phi_{\text{global}}) = 0 \quad \text{and} \quad -\Delta\phi_{\text{global}} = \rho_{\text{total}}/\epsilon_0,$$

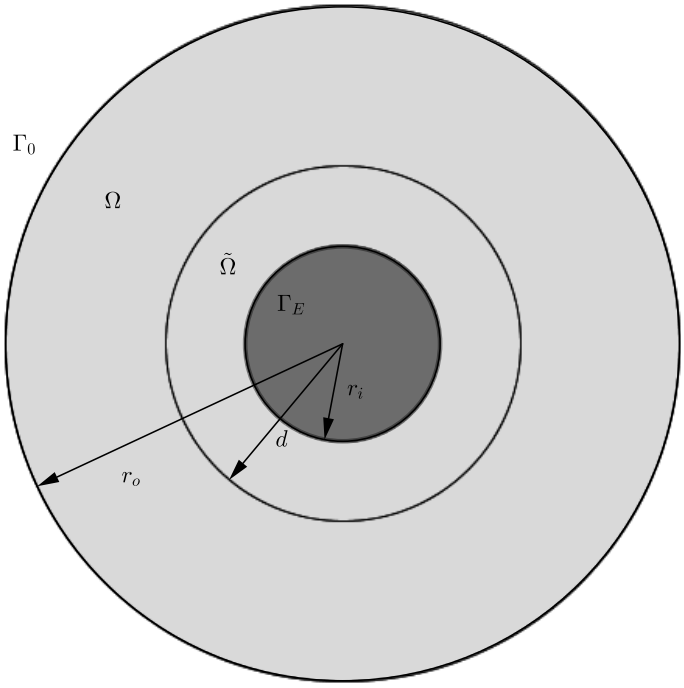

Figure 3.1: Illustration of a geometry with coaxial cylinders, with radii r_i and r_o. Ω denotes the region between the two cylinders and $\tilde{\Omega}$ extends slightly beyond the ionization region close to the inner cylinder, which occurs if the the inner cylinder is kept at a certain negative voltage compared to the outer cylinder.

in the full domain Ω. Furthermore, we want to solve:

$$\nabla \cdot (\mu_e \rho_e \nabla \phi_{\text{local}}) = k_i \rho_e - k_a \rho_e,$$

$$\nabla \cdot (\mu_p \rho_p \nabla \phi_{\text{local}}) = k_i \rho_e,$$

$$\nabla \cdot (\mu_n \rho_n \nabla \phi_{\text{local}}) = k_a \rho_e,$$

and

$$-\Delta \phi_{\text{local}} = \frac{1}{\epsilon_0}(\rho_e + \rho_p + \rho_n),$$

in $\tilde{\Omega}$, which encloses the ionization region. To make this set of equations yield the three-species solution in the full domain, we must in addition to the ordinary boundary conditions in the models, impose the following:

1. The charge density ρ_{total} must satisfy:

$$\begin{cases} \rho_{\text{total}} = \rho_e + \rho_p + \rho_n & \text{inside } \tilde{\Omega} \\ \rho_{\text{total}} = \rho & \text{inside } \Omega \backslash \tilde{\Omega}. \end{cases}$$

2. The potentials must satisfy:

$$\phi_{\text{local}} = \phi_{\text{global}} \quad \text{on} \quad \Omega^\circ \cap \partial\tilde{\Omega}.$$

3. The one-species charge density ρ must satisfy:

$$\rho = \rho_n \quad \text{on} \quad \Omega^\circ \cap \partial\tilde{\Omega}.$$

As the solution procedure for the solvers in Chapter 2 is iterative, we will satisfy the boundary conditions by making interleaved iterations with the global and local solvers, using the solution that is not updated to set boundary conditions. To satisfy (1), we will use the charge density from the local solver when we assemble the residual in the Newton algorithm in the region $\tilde{\Omega}$. Furthermore, as we do not want ρ to affect the potential inside $\tilde{\Omega}$, we modify the discretization in this region. The details for this are given in Section 3.2. To satisfy (2), we interpolate the solution in the global solver to the boundary of the local solver and set a Dirichlet boundary condition as described in Section 3.3. Finally, to satisfy (3), we either set a boundary condition for the charge density at the physical boundary or at an artificial boundary that extends into the domain. In the former case, we use the method of characteristics to solve the one-species problem to the boundary Γ_E. The details will be given in Section 3.4. Regarding the latter case, we refer to Section 3.5.

3.2 Modification of the Newton algorithm

To avoid ρ from affecting the potential in the ionization region, the discretization of the equation for the potential in (2.5) is replaced by:

$$-\int_{\partial V} \nabla\delta\phi \cdot \mathrm{d}S = \int_{\partial V} \nabla\phi \cdot \mathrm{d}S + \int_V \frac{1}{\epsilon_0}\rho_{\text{total}}\mathrm{d}V. \tag{3.1}$$

When we consider applications, the local solver will use a mesh that is an annulus and we introduce a radial cut-off r_c such that we use this alternative discretization for cells with centers that are closer than r_c, to the center of the annulus. Note that r_c must be chosen to be sufficiently large so that the defined volume includes the ionization region.

3.3 Interpolation of charge densities and the electric field

Interpolation must be performed when setting boundary conditions by using solution quantities from different meshes. In the global solver, the potential is interpolated to the boundary of the local solver. This is performed by using trilinear interpolation [16, 15], first to the nodes and then to the point of interest. A motivation for this procedure is that it results in a continuous interpolant at the nodes (as well as faces) of the cells, which would not be the case if e.g. face values were used to interpolate the potential.

In the local solver, the charge density as well as the magnitude of the electric field may need to be interpolated. Similarly as in the structured case, we first interpolate the solution to the vertices of the triangle which contains the intended interpolation point. The values Φ_{v_i} at the vertices v_i are defined by using inverse distance averaging:

$$\Phi_{v_i}\left(\sum_T \frac{1}{d(T,v_i)}\right) = \sum_T \frac{\Phi_T}{d(T,v_i)}, \tag{3.2}$$

where T ranges over all triangles that share the vertex v_i and $d(T,v_i)$ denotes the distance between this vertex and the center of triangle T. By using the vertex values it is then possible to calculate the value at an arbitrary point in the triangle, according to:

$$\Phi = \xi_1\Phi_{v_1} + \xi_2\Phi_{v_2} + \xi_3\Phi_{v_3}, \tag{3.3}$$

where (ξ_1,ξ_2,ξ_3) denotes the barycentric coordinates for the interpolation point.

3.4 Boundary condition for the single-species charge density at the physical boundary

Observe that the equation for the one-species charge density can be written as:

$$n \cdot \nabla\rho + \frac{\rho_{\text{total}}}{E\epsilon_0}\rho = 0, \tag{3.4}$$

where n is the direction of the electric field. The left term can be viewed as the derivative along n and we may hence write:

$$\frac{\mathrm{d}\rho}{\mathrm{d}n} + \frac{\rho_{\text{total}}}{E\epsilon_0}\rho = 0, \tag{3.5}$$

which has the solution:

$$\rho(s) = \rho_0 \exp\left(-\int_0^s \frac{\rho_{\text{total}}(u)}{E(u)\epsilon_0}\,\mathrm{d}u\right). \tag{3.6}$$

Here, s parametrizes the length of the field-line and ρ_0 is an initial condition at $s = 0$.

To use this to set a boundary condition for ρ at a given point on the physical boundary Γ_E, we can map the field-lines a given distance d such that the final position resides outside the ionization region and evaluate (3.6) along this path with ρ_0 taken to be the value of ρ_{total} at the final position. This is done by approximating the integral in the exponent by a Gaussian quadrature rule:

$$\int_0^d \frac{\rho_{\text{total}}(u)}{E(u)\epsilon_0}\,\mathrm{d}u = \sum_{i=1}^{n} \omega_i \frac{\rho_{\text{total}}(u_i)}{E(u_i)\epsilon_0}, \tag{3.7}$$

where u_i and ω_i are determined by properties of the Legendre polynomials. Such quadrature rule integrates polynomials of degree $2n-1$ exactly and is suited if the integrand can be accurately represented as a polynomial. In addition to the evaluation of the integral we need to determine sequences of points $x(u_i)$ along field-lines of interest. This is done by recursively taking steps:

$$x(u_i) = (u_i - u_{i-1})n_{i-1} + x(u_{i-1}), \tag{3.8}$$

where n_i is the normalized direction of the electric field at $x(u_i)$, $u_0 = 0$, $u_{n+1} = d$ and $x(u_0)$ is the boundary point of interest.

Finally, note that the evaluation of solution quantities along field lines involves search for the triangle to which a given point belongs. This may either be performed occasionally, with a list of triangle indices and coordinates $x(u_i)$ to speed up the evaluation, or each time a boundary condition must be evaluated. In the implementation for the unstructured solver, we use the former alternative. The mentioned list is then updated for a decreasing sequence of thresholds for the total relative update in Section 2.3.

3.4.1 Accuracy in the one-species boundary condition and parameter selection

To perform calculations in the domain decomposition approach where we set a boundary condition at the physical boundary, one must specify the distance d that shall be traced along the field-lines and the number of quadrature points n. Here, we will use the geometry with coaxial cylinders and a three-species solution that has been obtained from a one dimensional finite element solver, to analyze the effect of various choices of d and n.

To begin with, we consider the single-species solutions that are obtained when the boundary condition for the single-species solver is calculated with different values of d. This is shown in Figure 3.2, which also includes the total charge density from the three-species model. The values that were considered for d are given by 2 mm, 2.25 mm, 2.5 mm and 2.75 mm, yielding positions that are slightly beyond the peak in the total charge density in the three-species model, which identifies the ionization region. The figure shows that, for these values of d, there is no discernible difference in the obtained single-species solution for the charge density.

A convergence study has been performed regarding the accuracy in the boundary condition that is obtained for different numbers of quadrature points. Figure 3.3 shows the relative

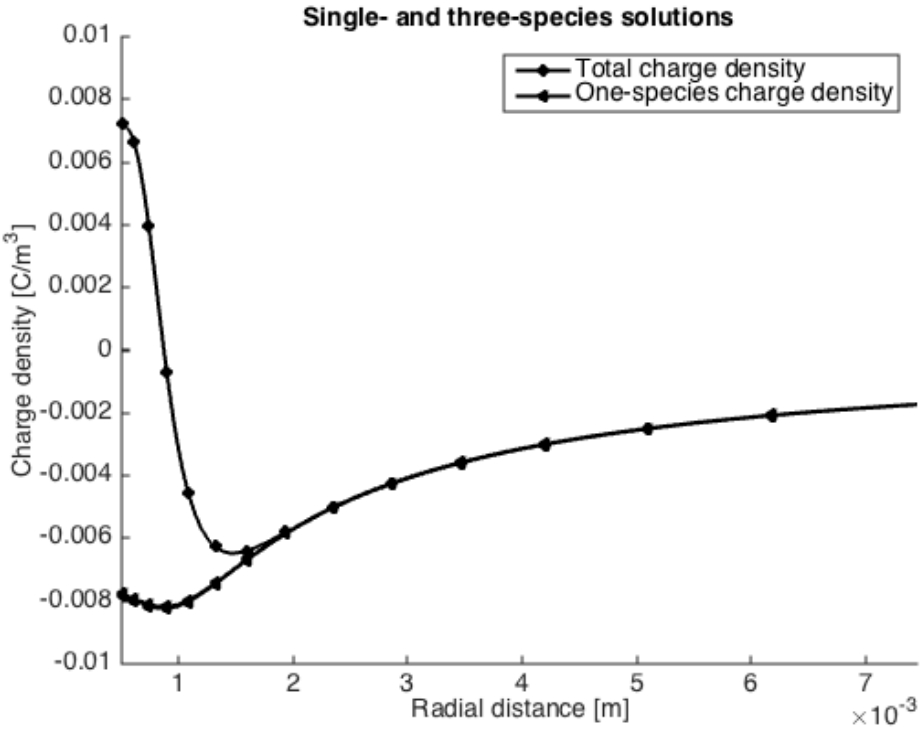

Figure 3.2: The one-species charge densities corresponding to the boundary conditions that are implied by the method of characteristics, for field-lines extending distances of 2 mm, 2.25 mm, 2.5 mm and 2.75 mm into the domain. All of these are shown with the same marker and as can be seen, there is no discernible difference for the different values of d. The figure also includes the total charge density, according to the three-species model. The applied voltage between the cylinders is -12 kV.

difference in the boundary condition when increasing the number of quadrature points. As can be seen; using four or more quadrature points yields an accuracy of 1 % or better.

3.5 Boundary condition for the single-species charge density at an artificial boundary

Similarly to what was done in Section 3.2, we introduce an annulus with outer radius r_c which encloses the ionization region. The outer boundary of this annulus is implemented as an immersed boundary, i.e. following the description in Section 2.2, and a boundary condition for the negative ion charge density is obtained by interpolation of the local three-species solution, using the procedures that were described in Section 3.3.

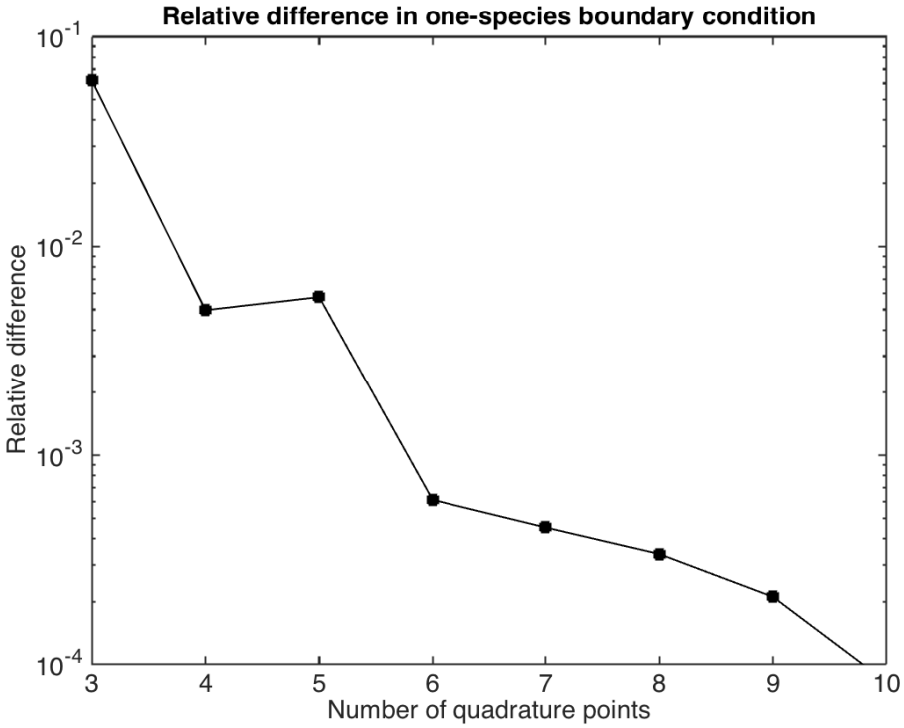

Figure 3.3: The relative difference in the boundary condition for the charge density in the one-species model as a function of the number of quadrature points, for a geometry with a pair of coaxial cylinders.

Chapter 4

Validation of implemented solvers and approach with domain decomposition

This chapter validates the implemented three-species solvers by considering results in geometries with coaxial cylinders. These geometries are one dimensional and accurate reference solutions can been obtained by using a one-dimensional finite-element solver [10].

Initially, we verify the implemented unstructured three-species solver in cartesian coordinates. This is performed by considering a pair of coaxial cylinders with dimensions $r_i = 0.5\,\mathrm{mm}$, $r_o = 3.765\,\mathrm{mm}$ and the applied voltage $V_E = 8\,\mathrm{kV}$, where the notation is in accordance with Figure 1.1. In addition to verifying that the solution from the unstructured solver agrees with the one-dimensional counterpart, we make an analysis of convergence with respect to mesh size.

After establishing the correctness of the implemented unstructured three-species solver in cartesian coordinates, we turn the attention to the domain decomposition approach. Here, we consider a validation case with a slightly larger outer cylinder with radius $r_o = 7.5\,\mathrm{mm}$ and the applied voltage $V_E = 12\,\mathrm{kV}$. The use of a test case with larger outer cylinder is motivated by that the smaller geometry does not exhibit a region that essentially is dominated by one species. We validate both approaches, that were described in Chapter 3, to couple a local three-species and global one-species solver.

Finally, we note that we will in this presentation neglect the discussion of convergence with respect to the choice of iterative cut-off. Investigations regarding this issue have been performed in [10], where the accuracy was deemed sufficient when the relative update of the solution had fallen below 10^{-4}.

Table 4.1: The relative l^2-difference between solutions at consecutively finer meshes for the unstructured three-species solver in cartesian coordinates. Here, the mesh size refers to the size of the triangles close to the inner cylinder.

Number of triangles	Mesh size [μm]	ϕ	ρ_e	ρ_n	ρ_p
38316	7.50	-	-	-	-
150386	3.75	0.0003	0.0545	0.0345	0.0425
595042	1.88	0.0001	0.0380	0.0250	0.0317

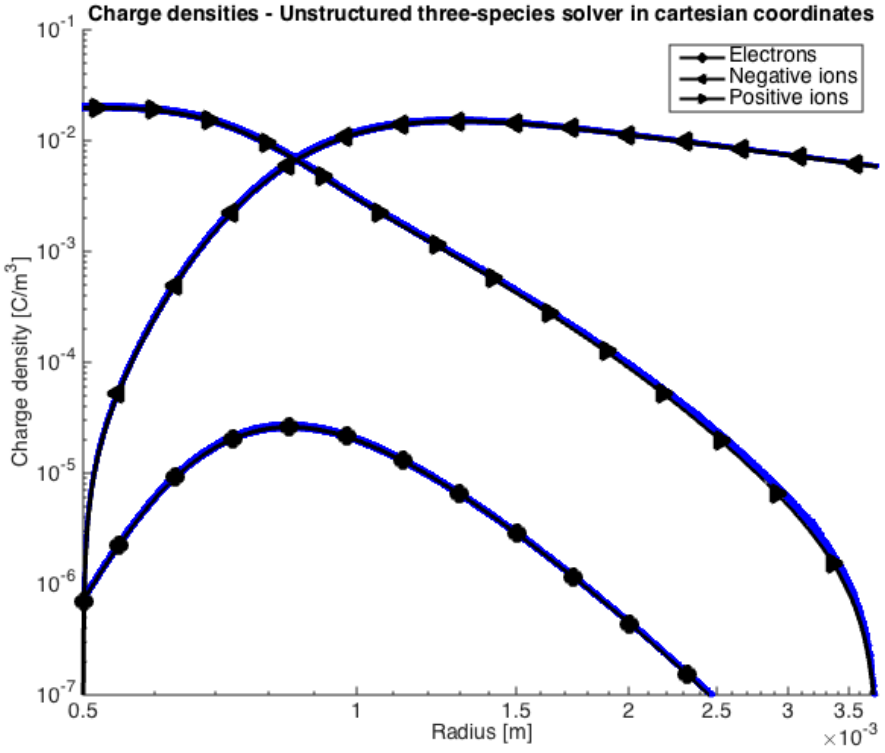

Figure 4.1: Charge densities in a geometry with a pair of coaxial cylinders, calculated by using the two dimensional unstructured three-species solver in cartesian coordinates (blue) and a one-dimensional finite-element solver (black).

4.1 Validation of two-dimensional unstructured finite volume three-species solver in cartesian coordinates

Figure 4.1 shows the solution for charge densities in the validation case, calculated with the implemented unstructured finite volume solver in cartesian coordinates. The solution has been

calculated using a mesh with 595042 triangles and a mesh size of 1.88 μm at the inner cylinder. In the figure, we have also included the charge densities according to a solution from the previously mentioned one-dimensional three-species solver. The relative difference in l^2-norm between the one- and two-dimensional solution is 0.07 % for the potential, 2.5 % for the electron charge density, 1.7 % for the negative ion charge density and 2.1 % for the positive ion charge density. As can be seen from the figure, much of these errors can be attributed to the noise level in the two dimensional solution.

To investigate convergence with respect to mesh size, we have calculated the relative difference in l^2-norm for solutions at three consecutively finer meshes. Table 4.1 shows the results and it may be concluded that a mesh size in the range between 1.0 μm and 10.0 μm at the inner cylinder, yields an accuracy of within a few percent.

4.2 Validation of domain decomposition approach

In Figure 4.2, we show the solution for charge densities in the validation case, for the two different approaches with domain decomposition. In both cases, the mesh for the local solver extended a distance 3.765 mm into the domain, with a mesh size of 1.88 μm at the inner cylinder. Furthermore, the coupling between the potential and charge density for the Newton solver was suppressed for radial distances less than 3.0 mm from the center of the cylinders. For the approach where the boundary condition is set on the physical boundary, the field-lines were traced a distance of 2.5 mm. To evaluate the boundary condition at the inner cylinder, six quadrature points were used. According to Chapter 3 this should give rise to an error of less than 0.1 % due to the integration, which for meshes of similar type as in Section 4.1, can be neglected. Regarding the approach with an artificial boundary, this boundary was located at a distance of 3 mm from the center of the cylinders, i.e. the same boundary to which the previously mentioned field-lines extended. Finally, regarding the mesh size for the global solver, we used the uniform grid-spacing 0.1 mm, with two refinement levels close to the inner cylinder.

As can be seen from Figure 4.2, the charge densities that are calculated by a coupled local and global solver agrees qualitatively to the one-dimensional counterparts. To give a quantitative measure of the accuracy, we calculate the relative difference in l^2-norm between the negative ion charge density in the reference solution and the solution obtained by the global one-species solver for radial distances larger than 3.0 mm. In the case where we set a boundary condition for the single-species charge density at the physical boundary, we get the relative l^2-difference 1.34 %, whereas we get 2.55 % when the boundary condition is set at an artificial boundary. It appears that we, for the given meshes, get a slightly better accuracy when setting the boundary condition at the physical boundary than on the artificial boundary inside the domain. On the other hand, this does not imply any conclusion about which method is to be preferred as they put rather different restrictions on the choice of the single-species mesh.

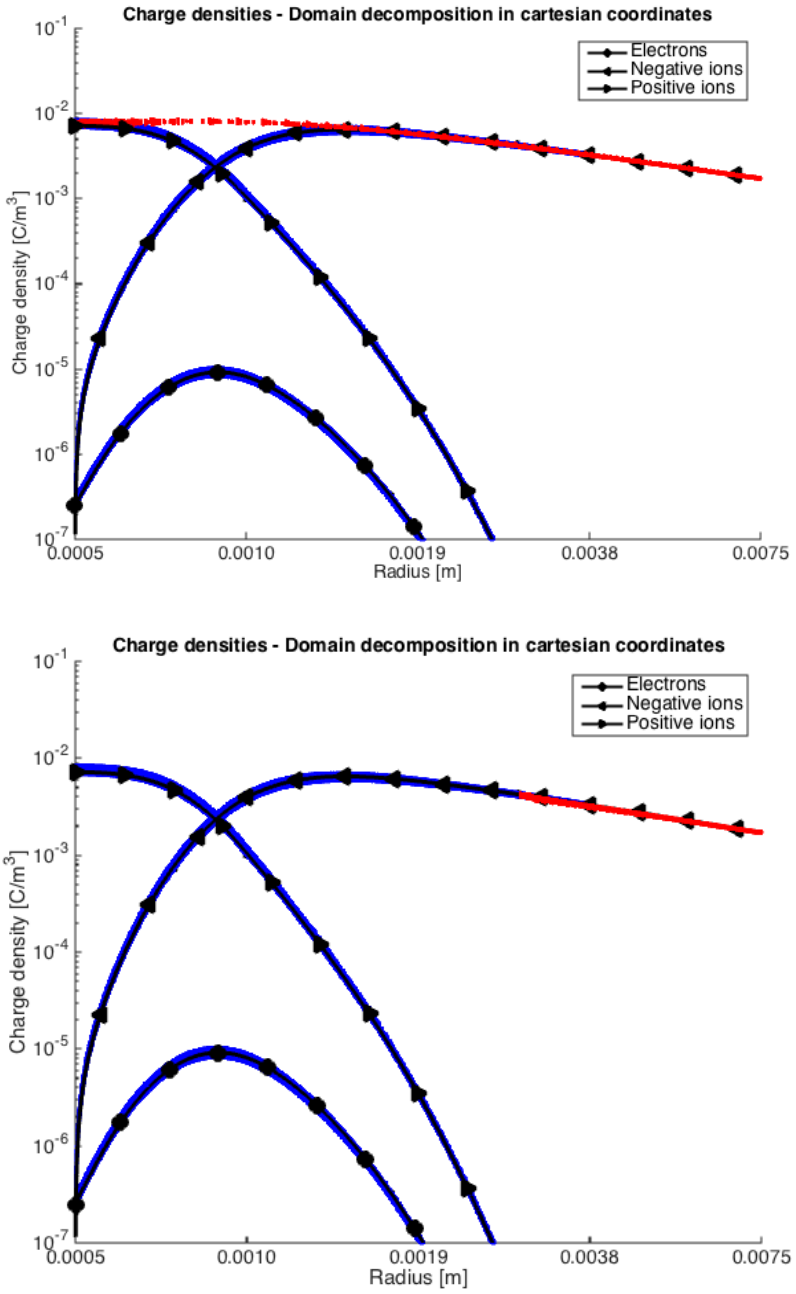

Figure 4.2: Charge densities that are calculated using the domain decomposition approach, with different approaches to set the boundary condition for the one-species charge density. The upper illustration corresponds to the case with a boundary condition that is set on the physical boundary whereas the lower illustration corresponds to the use of an artificial boundary. The one dimensional reference solutions are black, the one-species solutions are red and the local three-species solutions are blue.

Chapter 5

Applications of the domain decomposition approach

In this chapter, the aim is to apply the developed code to analyze negative corona discharge phenomena in geometries that are connected to industrial applications. We will consider two examples, one which is of interest to electrostatic precipitators and one that concerns automotive spray painting. In the former case, we consider a setup with wires between parallel plates, which is illustrated in Figure 5.1. When presenting the results, we will especially put focus on the single-species solution, i.e. the negative ion charge density and electric field, which is essential for the charging and transport of polluting particles in the air flow of an electrostatic precipitator. This forms the basis for the discussion in Chapter 6, where we determine the particle collection properties of electrostatic precipitators.

Regarding the application to automotive spray-painting, we treat multipole geometries similar to the ABB G1 rotary spray bell. This geometry consists of six needles (sharp tips) that are arranged in a regular hexagon and held at a negative potential relative to a needle at the origin. As this is a purely three-dimensional geometry, we will not be able to study it by using the two dimensional local three-species solver in this thesis. Instead, we will make a two-dimensional analogy, where the needles have been replaced by wires. The resulting geometry is shown in Figure 5.2 and the wires will only exhibit a partial corona region in the direction of the grounded wire. We consider this geometry as well as counterparts with different numbers of wires. Based on this, we discuss the possibility to use the three-species solution to parametrize boundary conditions for a one-species solver. This is of interest to simulations that optimize automotive spray painting, where the use of the three-species model is too computationally demanding. Instead, one wants to set a boundary condition for the negative ion charge density for a single-species solver at a boundary that possibly is slightly larger than the physical boundary of the wires.

Finally, note that by making the above mentioned examples, we wish to illustrate that the approach with domain decomposition manages to make accurate three-species calculations in geometries that are orders of magnitude larger than the scale of the corona phenomena and

hence makes the method feasible for industrial applications.

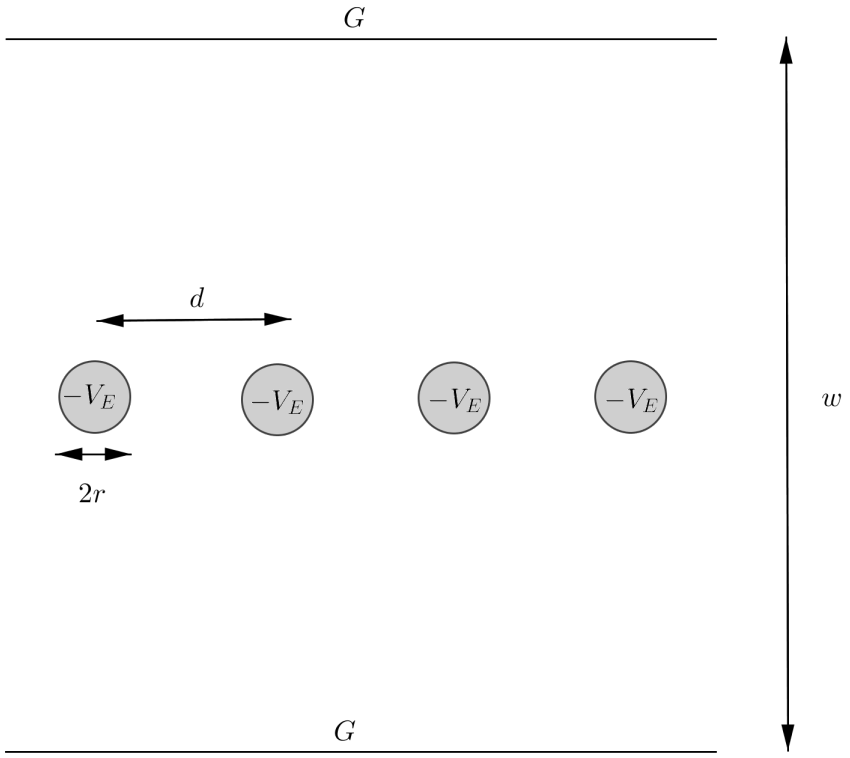

Figure 5.1: Electrostatic precipitator with periodically positioned wires between a pair of collector plates (marked G). The wires, with radii r, are separated by a distance d and associated with the potential $-V_E$. The width between the pair of grounded collector plates is denoted w.

5.1 Parallel plate electrostatic precipitators

5.1.1 Geometrical configuration

Figure 5.1 illustrates a parallel plate geometry for an electrostatic precipitator. We have a sequence of wires of radius r that are placed in the middle, between two parallel plates, at a distance d from each other. The plate to plate distance is given by w and there is a negative voltage $-V_E$ that is applied between the wires and the plates. Here, we will take

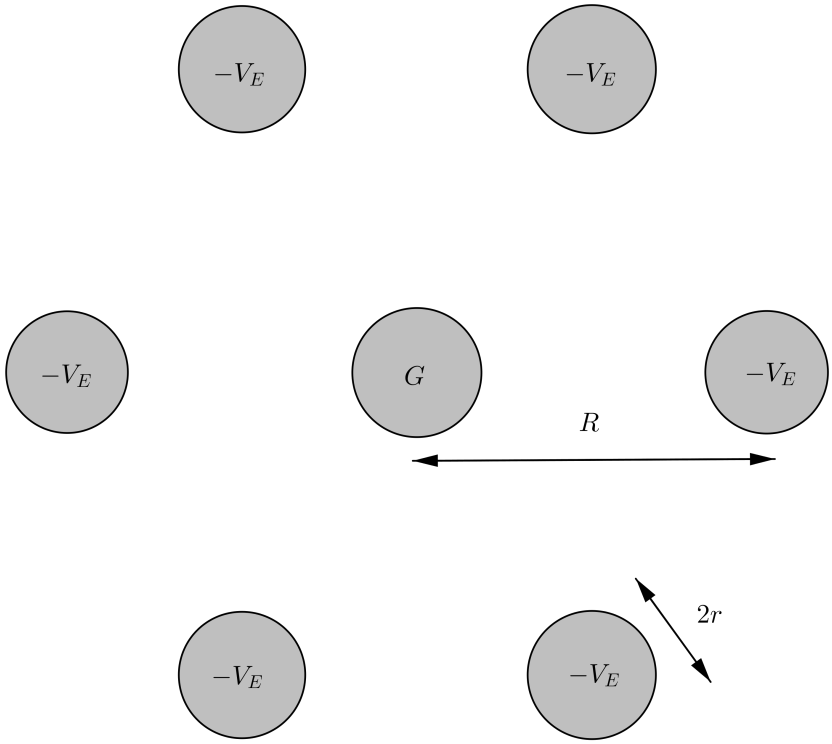

Figure 5.2: Two dimensional analog of the ABB G1 rotary spray bell, where the needles have been replaced by wires. There are six wires with voltage $-V_E$ and radius r that have been placed at the corners of a regular hexagon, at a distance R from a grounded wire (marked G) at the origin.

$r = 0.5\,\text{mm}$ and $w = 0.5\,\text{m}$. Furthermore, we will consider a range of different wire-wire separation distances, namely $d = 5\,\text{cm}$, $10\,\text{cm}$, $15\,\text{cm}$, $20\,\text{cm}$, and $25\,\text{cm}$. These correspond to the applied voltages $V_E = 70\,\text{kV}$, $40\,\text{kV}$, $35\,\text{kV}$, $30\,\text{kV}$, and $30\,\text{kV}$. The use of different applied voltages is motivated by that the necessary voltage to obtain a steady state corona solution increases as the distance between the wires decreases. Furthermore, in the simulations, we consider an electrostatic precipitator with three periodically identical wires. In this particular case, however, the symmetry of the problem would have allowed us to consider a setup with only one wire. On the other hand, in geometries that occur in industrial applications it is common that the bounding box is less symmetrical, which makes it necessary to include more wires in the simulation. Finally, it can be mentioned that the solutions were iterated until the relative update had fallen below 10^{-3} for each local solver.

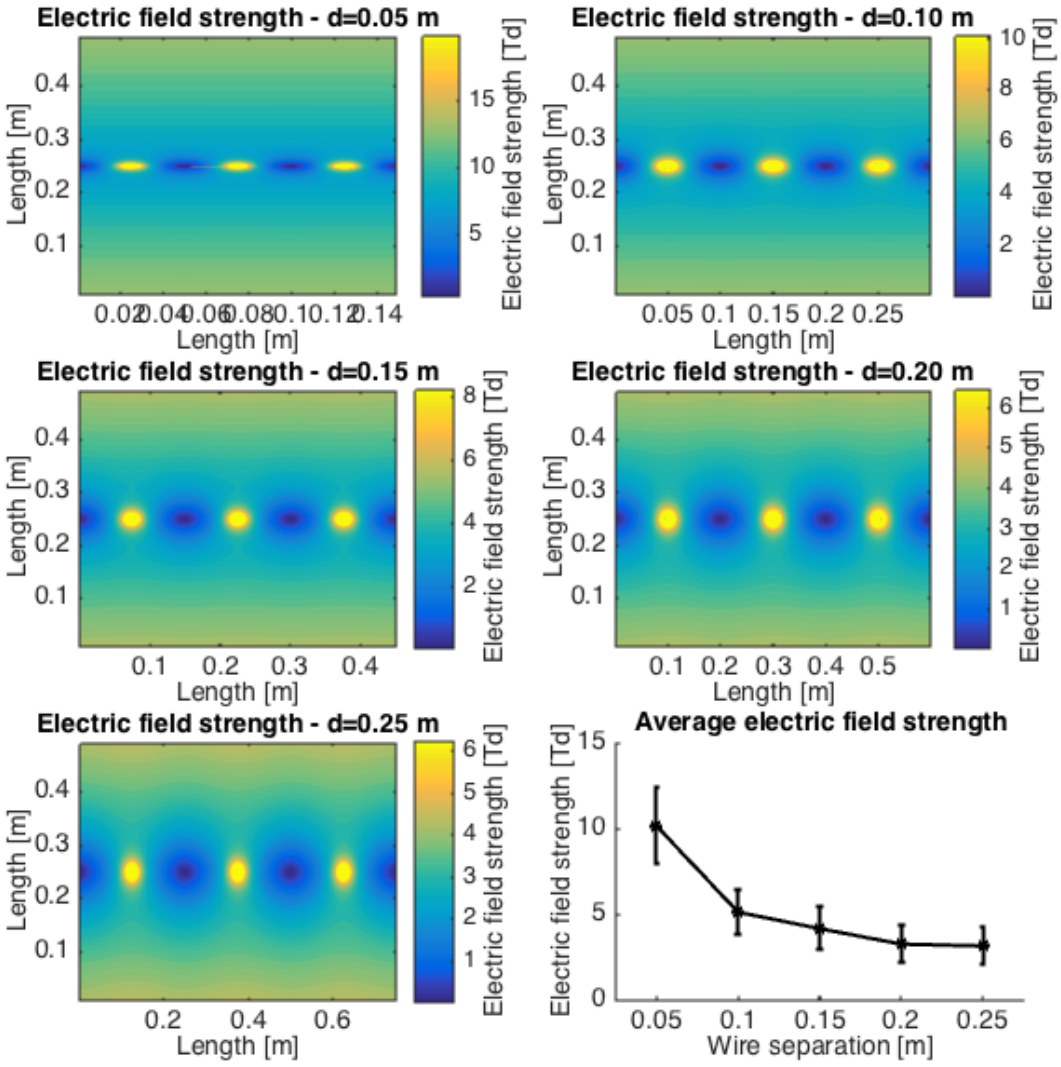

Figure 5.3: The electric field strength in a parallel plate electrostatic precipitator that contains three wires, for a number of wire-wire separation distances d. Note that the scale for the electrostatic field has been truncated. Due to this truncation, the electric field strength close to the wires takes the maximum value that is admitted by the scale. The lower right part of the figure shows the average electric field strength in the various geometries as a function of the wire-wire separation.

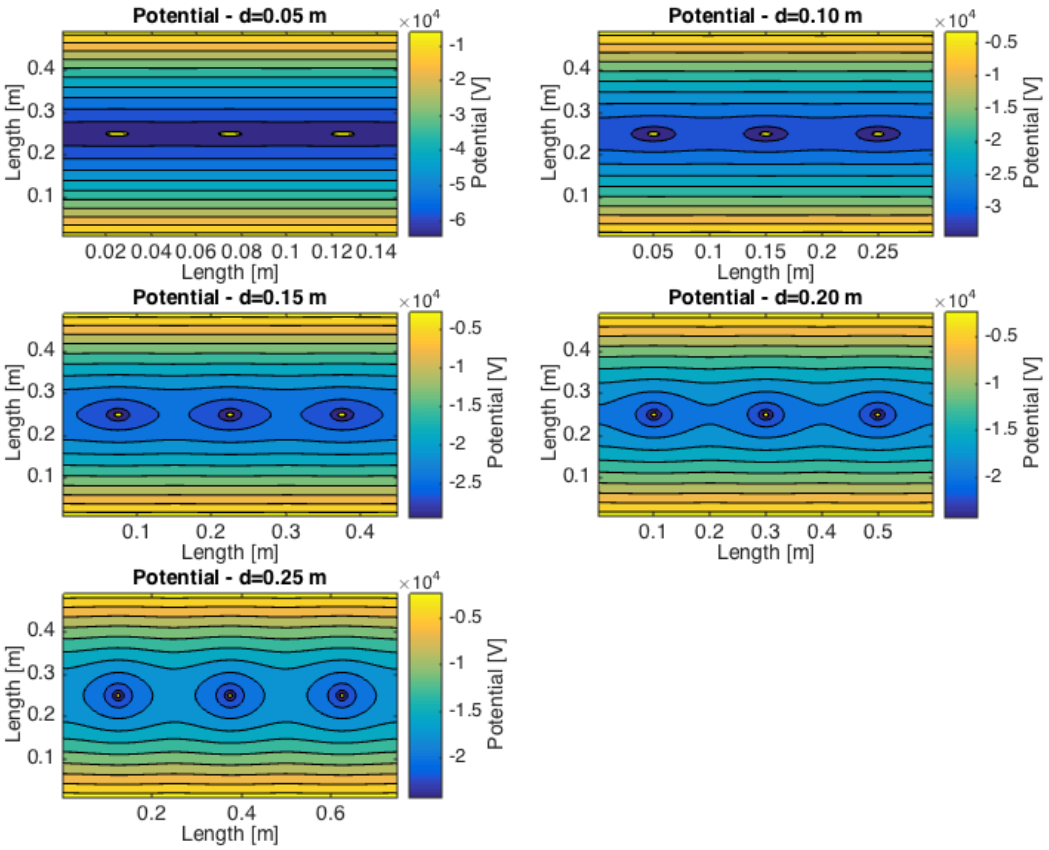

Figure 5.4: The potential in a parallel plate electrostatic precipitator that contains three wires, for a number of different wire-wire separation distances d. We have also included contour-lines to indicate the direction of the electric field.

5.1.2 Electrostatic properties

As previously mentioned, in Chapter 6, we consider particle collection properties for the electrostatic precipitator geometries that are presented in this chapter. Regarding this issue, the results from the electrostatic simulations primarily enter the problem through the model that describes the charging of polluting particles and the transport of charged particles. The maximum charge that a particle can gain is dependent on the electric field strength, and there is a time-constant for charging that depends on the charge density of negative ions. For the transport, we are obviously also interested in the direction of the electric field.

In Figure 5.3, we show the electric field strength for different wire-wire distances. The calculated electric fields are seen to exhibit the correct periodicity that can be expected from

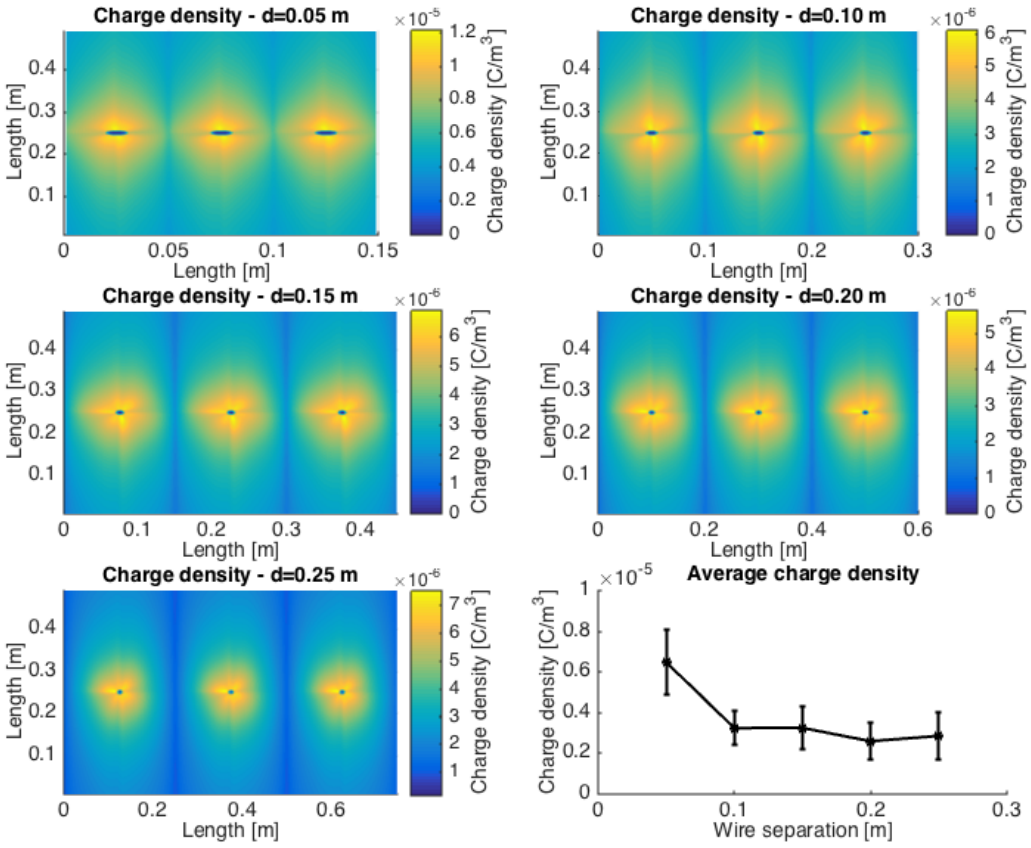

Figure 5.5: The charge density in a parallel plate electrostatic precipitator that contains three wires, for a number of different wire-wire separation distances d. The lower right part of the figure shows the average charge density in the various geometries as a function of the wire-wire separation.

the geometry. We also show the average electric field strength as a function of the wire-wire separation. With the chosen values for the potential, we get that the geometries with smaller wire-wire distances on average have slightly stronger electric fields. To obtain an efficient charging of particles, it is optimal to have a strong electric field in the parts of the domain that are occupied by particles. Furthermore, as the applied voltage has an upper and lower limit for which there exists a steady-state corona solution, it is beneficial if the electric field strength is as uniform as possible throughout the domain. Although further investigations need to be performed, this should, from a geometrical point of view, benefit the configurations with smaller wire-wire separation. In addition to this, Figure 5.4 shows the potential with contour lines to

indicate the direction of the electric field. As can be expected, shorter wire-wire separation leads to that the electric field is more directed towards the grounded planes.

Finally, Figure 5.5 shows the negative ion charge density for different wire-wire distances. In addition to this, the figure also shows the average negative ion charge density as a function of the wire-wire separation, which can be used to estimate the time constant for particle charging. It will be shown that this time constant is small compared to the residence time of a particle in the precipitator. Hence, the more detailed description of the spatial variations of the charge density is less important for the modeling of an electrostatic precipitator.

5.2 Multipole geometries

5.2.1 Geometrical configuration

As shown in Figure 5.2, we consider multipole geometries with wires that are arranged at the corner points of a regular polygonal structure, which is centered around a wire in the middle of the simulation box. The peripheral wires have radii $r = 0.5\,\mathrm{mm}$ and are located at a distance of $R = 11.5\,\mathrm{cm}$ from the center wire. The bounding simulation box has a side-length of one meter and is associated with a Neumann boundary condition. In this text, we consider geometries with one to six peripheral wires that are held at a negative potential compared to the grounded wire at the center.

Regarding the details of the geometrical configurations, the sides of the bounding box are alligned with the coordinate axes. The positions of the wires can then be written as:

$$\left(R\cos\left(n\Delta\theta+\theta_0\right), R\sin\left(n\Delta\theta+\theta_0\right)\right), \tag{5.1}$$

where n is an index for the wires, $\Delta\theta$ is given by $2\pi/N$ with N being the number of peripheral wires and θ_0 is an angular displacement. For $N = 1$ and 2, we take $\theta_0 = \pi/4$, but set $\theta_0 = 0$ otherwise.

Similarly to the case with parallel plate electrostatic precipitators, we obtain that the range of applied voltages, for which there is a steady-state solution, is strongly dependent on the geometry. For the different geometries with one to six peripheral wires, we used the voltages $V_E = 40\,\mathrm{kV}$, $60\,\mathrm{kV}$, $80\,\mathrm{kV}$, $100\,\mathrm{kV}$, $130\,\mathrm{kV}$, and $140\,\mathrm{kV}$. In Section 5.2.3, we will comment on the implications of these choices, with regard to the resulting electric field-strength at a contour that surrounds the wires. Finally, it can be mentioned that the solutions were iterated until the relative update had fallen below 10^{-3} for each local solver.

5.2.2 Examples of local and global solutions

Figures 5.6 and 5.7 show the negative ion charge density and potential for the multipole geometries with one to six wires; obtained by the global one-species solver. In all cases, we see that negative ions primarily are located along the connecting lines between the grounded wire and

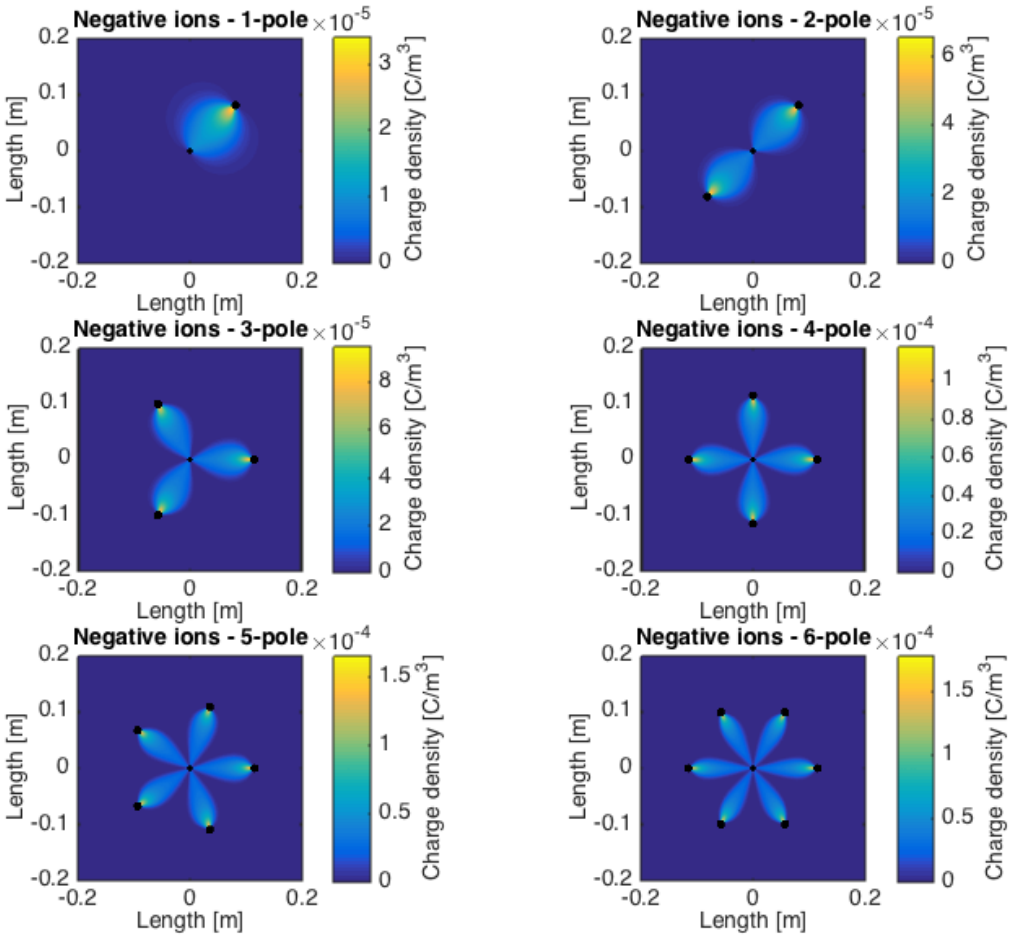

Figure 5.6: The charge density for negative ions, as calculated by the global solver, for multipole geometries with different number of wires. The wires are indicated by black dots and charge is primarily transported along the respective directions that connect the peripheral wires to the grounded center wire.

the wires that are held at a negative potential. Furthermore, both the solution for the negative ion charge density and potential appears to exhibit the symmetries that can be expected from the multipole geometry.

In addition to the negative ion charge density and potential, that are obtained by the global one-species solver, we have charge densities for both positive and negative ions as well electrons, which have been calculated by using a local three-species solver. In the current calculations, these local solutions are defined in regions that extend a few millimeters from the center of

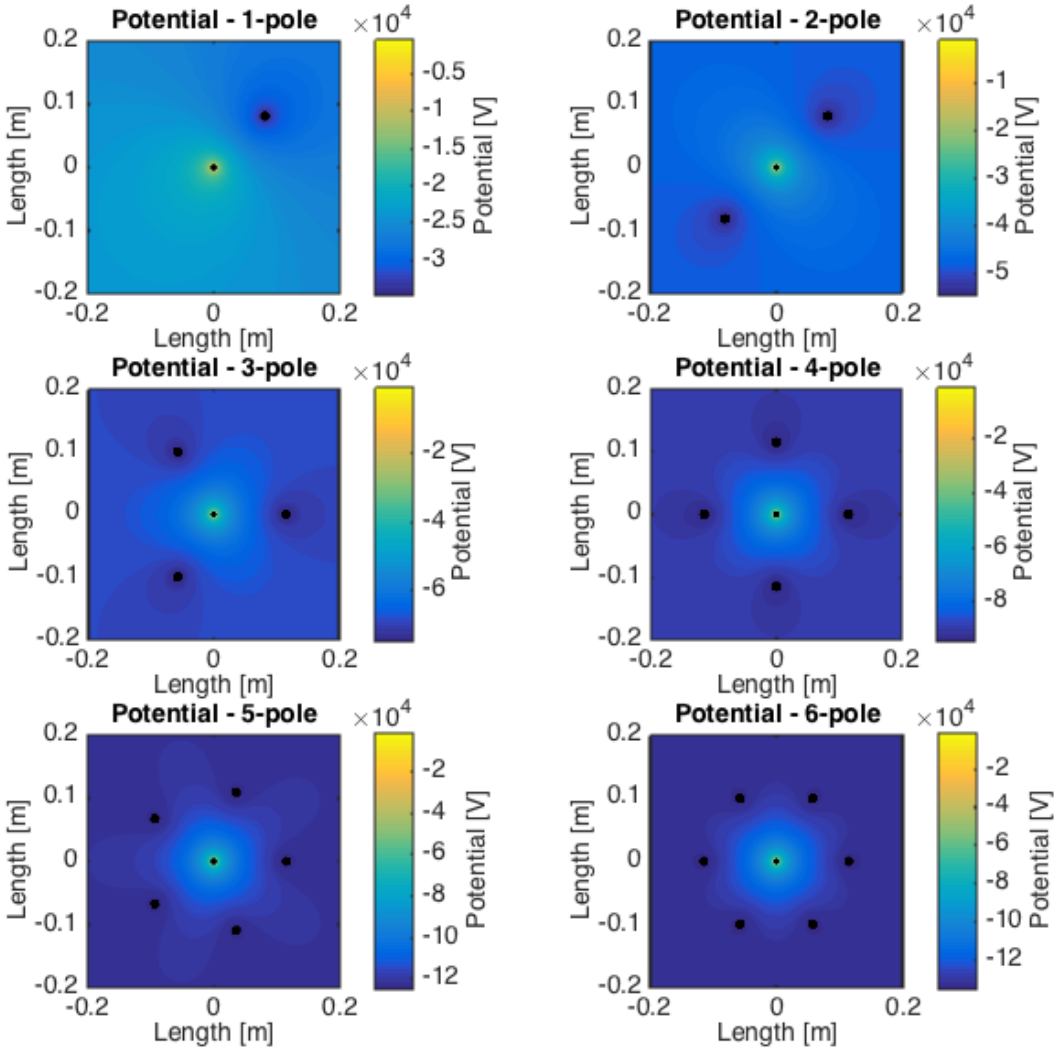

Figure 5.7: The potential, as calculated by the global solver, for multipole geometries with different numbers of wires. Note that the wires have been indicated by black dots.

the wires. We will not make an exhaustive study of local solutions, but limit our attention to the special case involving the wire $n = 0$, for the six-pole geometry. This is shown in Figure 5.8. We see that charged particles primarily are created by ionization and attachment in the direction of the grounded wire (to the left in the figure). In a similar way as in the validation case, the positive ion charge density has a maximum at the wire. Also, the electron charge

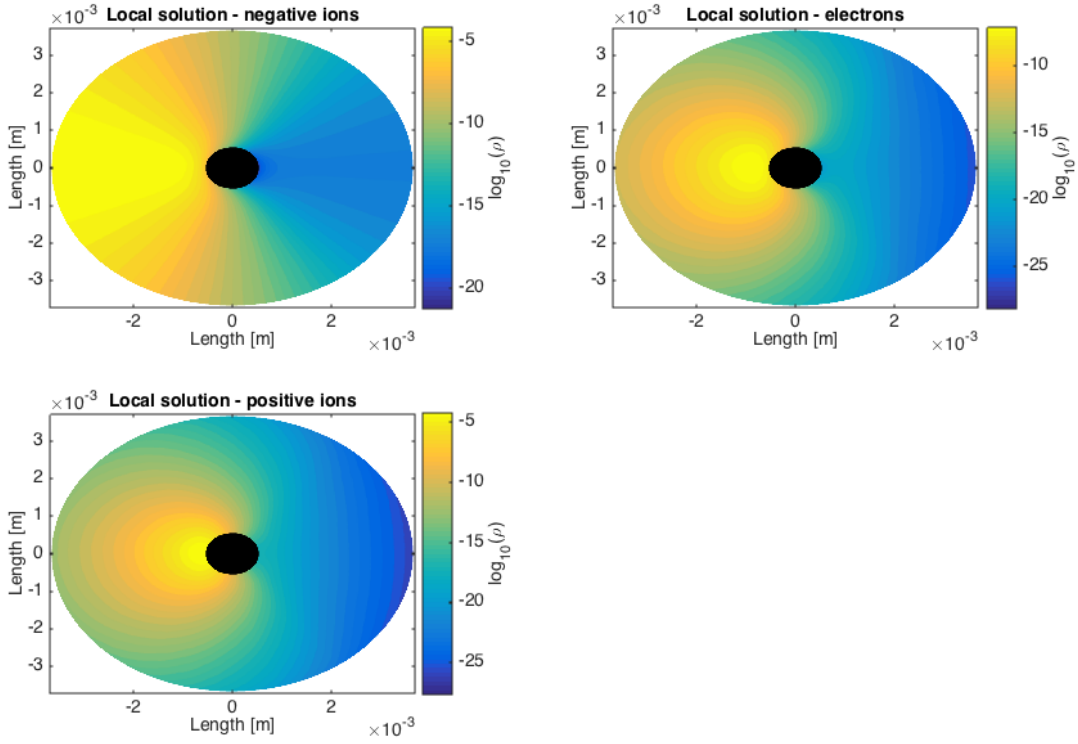

Figure 5.8: Showing charge densities for negative and positive ions as well as electrons, obtained from a local three-species solver, for the wire with $n = 0$ in the geometry with hexagonally arranged wires. As can be seen, the corona region is directed towards the left, i.e. towards the grounded wire, which is in agreement with Figure 5.6.

density exhibits a maximum slightly outside the wire, but vanishes beyond a short distance due to the formation of negative ions. This is in particular important as it indicates that the size of the local mesh is sufficient to resolve the presence of multiple species.

5.2.3 One species boundary condition at coronating boundary

As has been discussed in the introduction to this chapter, three-species simulations may be computationally too expensive to incorporate in multi-physics simulations of automotive spray painting. Instead, they are targeted at providing boundary conditions for the negative ion charge density for a one-species solver, at a boundary that surrounds the ionization regions (wires). To analyze the possibility of this, we consider the negative ion charge density at circular contours that surround the wires that are held at a negative potential. This is shown in Figure 5.9, for the different multipole geometries and a radius of $r_c = 1\,\text{cm}$ for the contour.

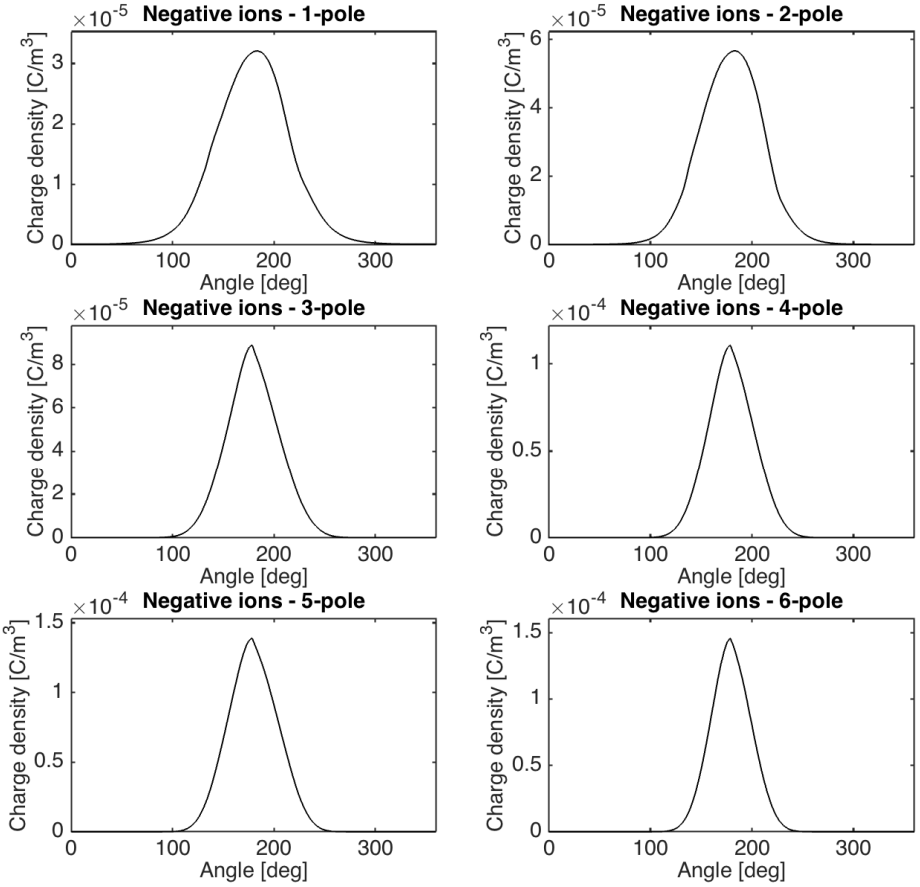

Figure 5.9: Showing the profile for the negative ion charge density at a circular contour with radius $r_c = 1\,\mathrm{cm}$, centered at the wire with $n = 0$, for the different multipole geometries.

In this figure, the solutions have been rotated such that the grounded wire at the center of the geometry is positioned at the angle $\theta = 180°$, which also is the direction in which the charge densities have their maximum values. As can be seen, the shape of the charge densities have a high degree of similarity and may be approximated by a Gaussian function:

$$\rho(\theta) = A \exp\left(-\frac{(\theta - \theta_0)^2}{B^2}\right), \tag{5.2}$$

where θ denotes the angular coordinate and A, B and θ_0 are constants. Clearly, B and θ_0 are quite similar for all cases, whereas the amplitude A is different. To be able to determine A, we need some empirical relation between the charge density and the one-species solution,

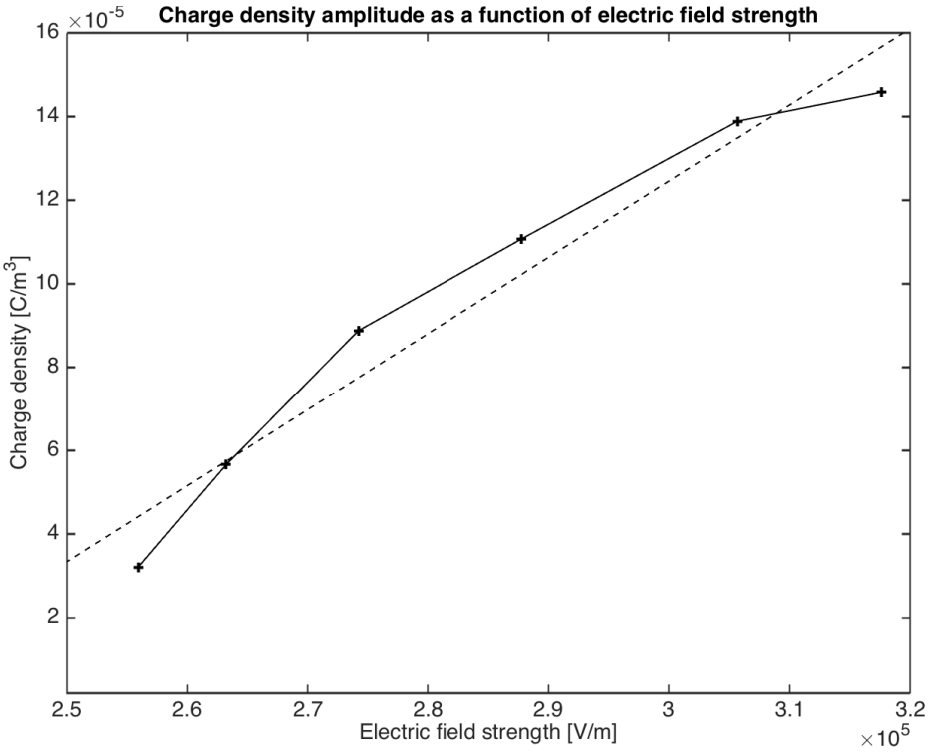

Figure 5.10: Showing the relation between the maximum charge density and electric field strength, for the different multipole geometries, at a circular contour with radius $r_c = 1\,\mathrm{cm}$, which is centered at the wire with $n = 0$. The maximum electric field strength at the contour was increasing with the number of wires, which can be used to identify the relation between the points and different multipole geometries.

possibly in combination with properties of the geometrical configuration. For example, a simple model would be to let A be a function of the maximum electric field-strength at the circular contour. This has been done in Figure 5.10, where the amplitude of the charge density profile can be seen to have a close to linear dependence on the electric field strength. This should give an indication that empirical parametrizations of a one-species boundary condition can be viable, although any such parametrization obviously depends on the choice of contour for the boundary condition.

Chapter 6

Applications to electrostatic precipitators

This chapter serves as a concluding detour into the application of three-species negative corona discharge simulations to electrostatic precipitators. We intend to determine particle collection properties for electrostatic precipitators, by tracing the paths of particles (e.g. ash-particles) that are subject to electrostatic- and fluid-forces. This has previously been studied in a range of different approximations [11, 19, 6, 14, 4]. A common approach is to use the Kaptzov criterion to set boundary conditions in a one-species model, when modeling the electrostatic properties. Here, we will, in contrast to these studies, use the results from the three-species simulations in Chapter 5 to parametrize boundary conditions for a one-species model.

In Figure 6.1, we illustrate the physics of an electrostatic precipitator in terms of a coupled fluid-, electrostatic- and particle-problem. For each pair of problems, we have a two-way coupling. The electrostatic field affects the fluid through the secondary electrohydrodynamic force and the negative ions are convected due to the velocity of the fluid. Regarding the particles and the electrostatic field, we have that the presence of negative ions causes charging of the particles, which hence makes them subject to an electrostatic force. At the same time, the presence of charged particles contributes to the space-charge and hence the electric field. Finally, the fluid affects the particles with a drag force which also gives rise to a counter-acting force on the fluid.

In the following simulations of electrostatic precipitators, some simplifications of the model have been made. Of the interactions in Figure 6.1, the electrostatic force, charging of particles and drag force must be included in any model of electrostatic precipitation. In addition to this, the secondary electrohydrodynamic force has been shown to have a significant effect on the flow, especially for lower air speeds [19, 6, 4, 21]. On the other hand, ion transport has a shorter time-scale than the convection due to the air flow, which hence can be ignored. Finally, in order for the inclusion of effects due to the presence of particles to be relevant, we need to determine relevant particle concentrations. This will typically be application dependent and we will in this work consider the limit with trace amounts of particulate pollution, which lets

us ignore these effects.

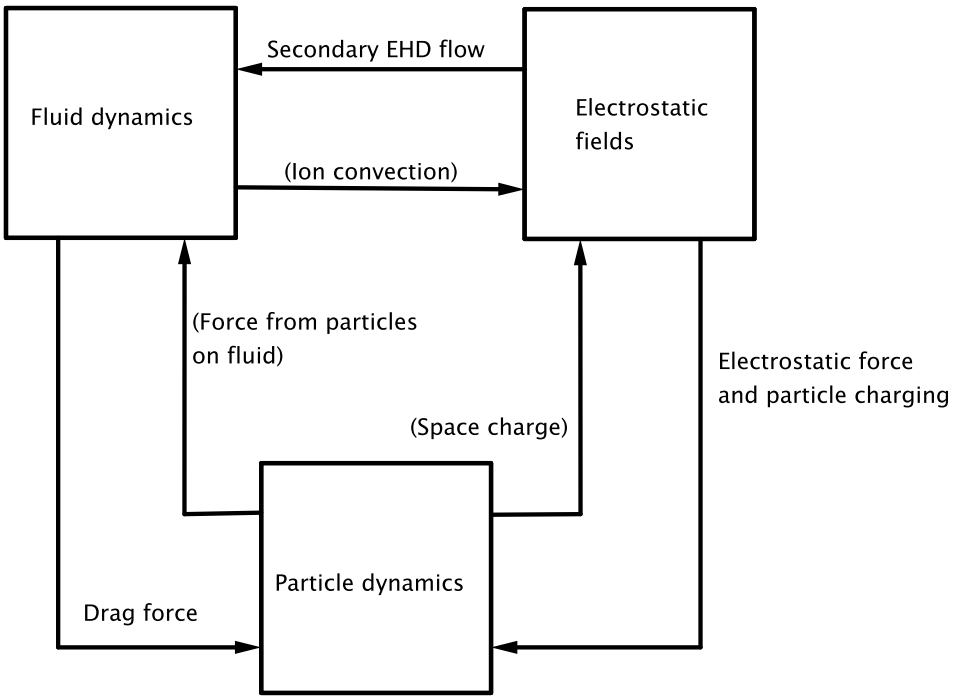

Figure 6.1: Schematic illustration of interactions between the fluid, electrostatic field and particles in an electrostatic precipitator. Interactions that are circumscribed by parentheses are not treated in the implemented model for electrostatic precipation.

6.1 Model for particle collection in an electrostatic precipitator

In this section, we outline some details regarding the described model for an electrostatic precipitator. Simulations have been performed using the multi-physics solver IBOFlow [16, 15]. This code contains functionality that previously has been used to simulate particles that are subject to electrostatic- and fluid-forces in connection to automotive spray-painting. Some adaptions of the code have been made to facilitate the simulation of electrostatic precipitators.

6.1.1 Geometrical setups

We consider the geometry with parallel plate electrostatic precipitators, which was shown in Figure 5.1. We will evaluate the particle collection properties for this kind of geometry for the different wire-wire separations that were considered in Chapter 5. In the previous chapter, we solely treated the electrostatic properties of the geometry. Here, we will also have an air flow through the electrostatic precipitator. More precisely, air will enter through the left boundary in Figure 5.1. To make the simulation results for the geometries with different wire-wire separation as comparable as possible, the total length of the plates in the direction of the air flow was taken to the same value 75 cm, in all cases. This means that the total number of wires in the simulation volume will be different in the various cases.

6.1.2 Electrostatic boundary conditions

To solve the electrostatic problem, we will use the previously discussed one-species solver. This solver needs a boundary condition for the negative ion charge density and potential at the wires. To obtain such boundary condition, we surround the wires by an artificial circular boundary with radius 5 mm, beyond which the one-species model is accurate. Boundary conditions for this boundary are then obtained by interpolation of the three-species solutions in Chapter 5.

6.1.3 Evolution of particles

Particles are introduced in the air flow at random uniformly distributed positions at the inlet boundary. When entering the simulation volume, their velocity is set to be the same as the velocity of the air flow. The particles have a slight variation in size, which follows a log-normal distribution. Furthermore, the particles are initially uncharged, but will subsequently be charged due to the presence of negative ions. The model for the charging process is based on [20, 26, 9]. Denoting the charge of a particle by Q, the model states that:

$$\frac{\mathrm{d}Q}{\mathrm{d}t} = \frac{Q_{\max}\tau}{(t+\tau)^2} \tag{6.1}$$

where $Q_{\max}$ is the maximum charge that can be acquired and is given by:

$$Q_{\max} = 3Er^2\pi\epsilon_0\left(\frac{\epsilon_r}{\epsilon_r+2}\right). \tag{6.2}$$

Here, E is the unperturbed electric field strength at the position of the particle, r is the radius of the particle and ϵ_r is the relative permittivity of the particle. In the following calculations, we take $\epsilon_r = 2$. Finally, the time-constant τ is given by:

$$\tau = \frac{4\epsilon_0}{\mu|\rho|}, \tag{6.3}$$

where ρ is the negative ion charge density and μ is the mobility constant for negative ions.

To give an indication about typical values for the maximum charge $Q_{\max}$ and time-scale for charging τ, we may consider the average values for the electric field strength and negative ion charge density that were presented in Chapter 5. Based on this, we deduce that $Q_{\max}$, for a particle of size $10\,\mu$m, is of the order of magnitude $10^{-15}\,$C and that τ is of the order of magnitude 10^{-2}-$10^{-1}\,$s. The latter value can be compared to the time-scale that is implied by the air speed in the electrostatic precipitator, which may be $1\,$m/s [6]. This indicates that the time-scale for particle charging is significantly shorter than the expected residence time in the electrostatic precipitator.

Finally, to evolve the particles, we integrate the equations of motion. The force term consists of contributions from the drag force and electrostatic force. In addition to this, turbulence effects are included based on an empirical model that was developed for simulations of automotive spray-painting [17]. The trajectory of a particle is either evolved until the particle hits a collecting plate or passes the outlet of the electrostatic precipitator. Based on this, the particle collection efficiency can be determined as the ratio between the total number of particles that have entered the domain and the number that have hit a collector plate.

6.2 Evaluation of particle collection properties for parallel plate electrostatic precipitators

In Figure 6.2, we show the particle collection efficiencies that were obtained for the parallel plate electrostatic precipitators, with different wire-wire separation distances. The results are based on simulation of $2 \cdot 10^5$ particles. The radial distribution was such that $\log(r)$ was normally distributed with mean value $\log(10^{-5})$ and standard deviation 1. Note that the mean value corresponds to the radius $r = 10\,\mu$m. Furthermore, the air speed was set to $1\,$m/s. The collection efficiencies are seen to range between $60\,\%$ and $90\,\%$. The geometries with shorter wire-wire distances are associated with higher particle collection efficiencies, which is probably associated with these having slightly stronger electric fields. Otherwise, the difference in collection efficiency is probably too small to draw any systematic conclusion regarding which geometry that is optimal. Since the maximum charge of a particle is proportional to the electric field strength, we get that the electrostatic force is proportional to the squared electric field strength. Hence, one may expect that the particle collection efficiency has a strong dependence on the applied voltage.

In addition to particle collection efficiencies, we present Figures 6.3 and 6.4, which show the distribution of the angle that is formed between the velocity vector of the particles and the collecting plates upon impact and the distribution of the particles at the outlet of the electrostatic precipitator. Whereas the angular distribution is quite similar for all geometries, there are larger amounts of particles close to the center of the outlet for the geometries with larger wire-wire separation. Hence, the acceleration of the particles towards the collecting plates

is less efficient for the geometries with these wire-wire separations. On the other hand, it is clear that in all cases, a substantial amount of the particles still have gained a velocity component that is directed towards a collecting plates and if the length of electrostatic precipitator would have been extended, these particles could have been collected as well.

Finally, note that the geometries for parallel plate electrostatic precipitators that were considered here, have a slightly larger plate to plate distance than what commonly occurs in other studies. The particular choice of plate to plate distance was inspired by a design that occurs in industry. A consequence of this is that the obtained particle collection efficiencies are difficult to compare to those in other studies. For example, Farnoosh et al [6] use a plate to plate distance of 10 cm and observe particle collection efficiencies of above 99 %, whereas the collection efficiencies in this study are significantly lower. Evidently, the larger plate to plate distance can be an explanation for this. Furthermore, the applied voltages in this study were not optimized to be as high as possible. They were chosen rather arbitrarily within the range for which there exists a steady-state corona solution in the three-species model. In the purely one-species model that is used by Adamiak et al, there are less restrictions on the choice of the applied voltage.

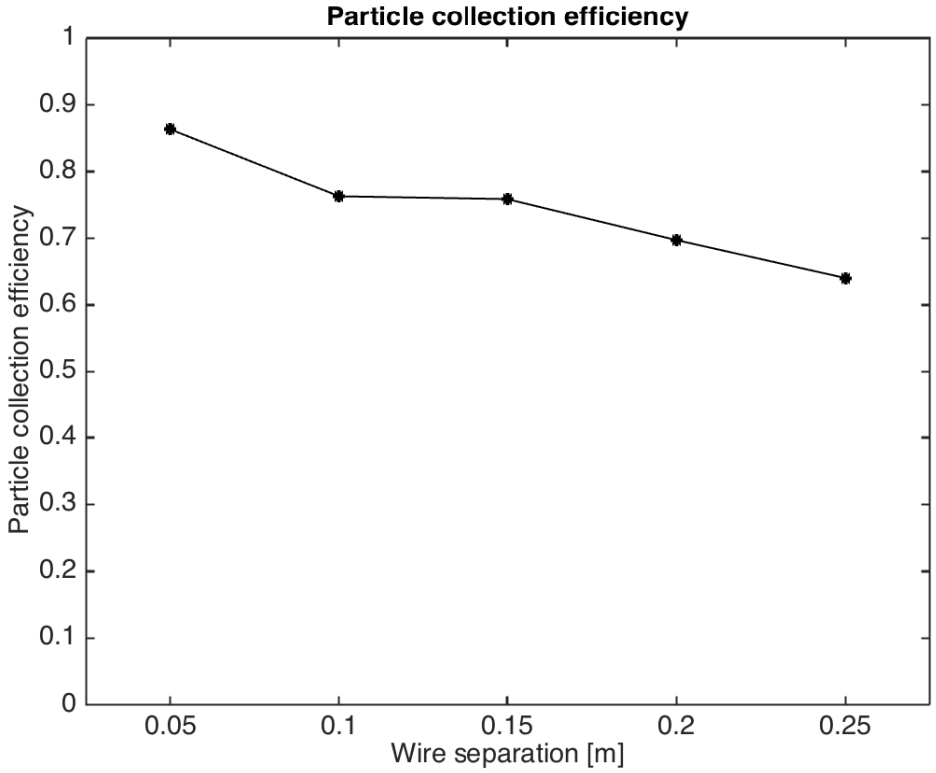

Figure 6.2: The particle collection efficiency, i.e. the quotient of the number of particles that has been collected at the grounded boundaries and the total number of particles that has entered the electrostatic precipitator, for configurations with different separation length between the wires.

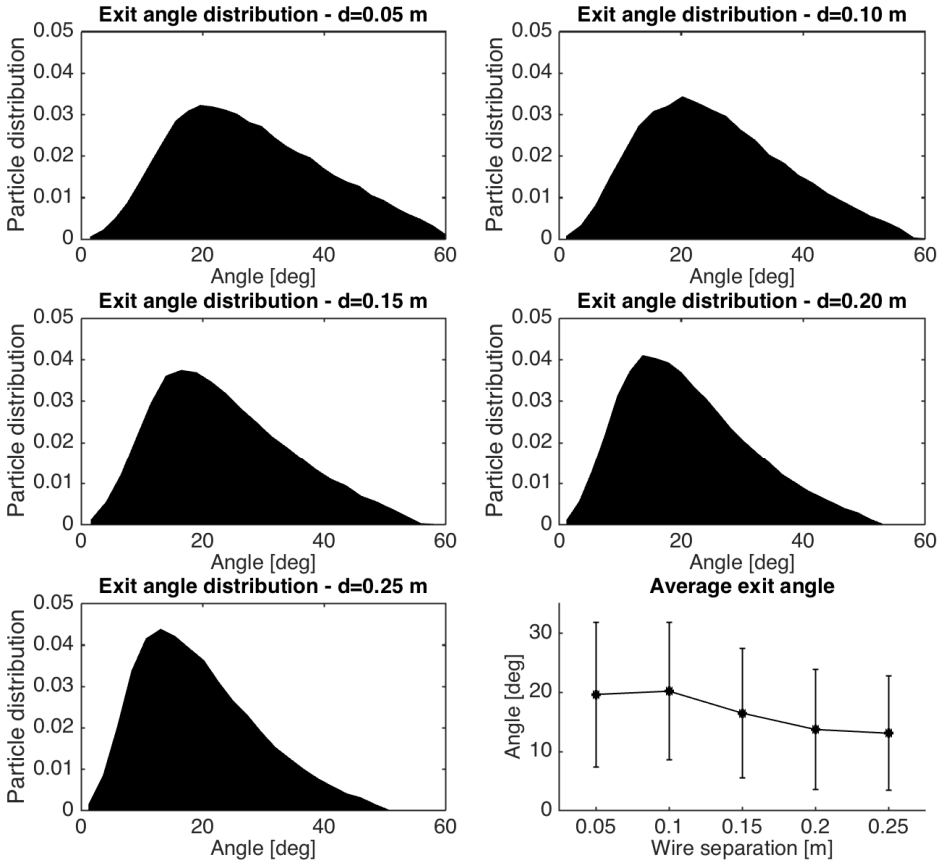

Figure 6.3: The angle between the velocity vector of the particles and the the collecting plate when the particles impact and hence are collected at the plate, for configurations with different separation lengths d between the wires.

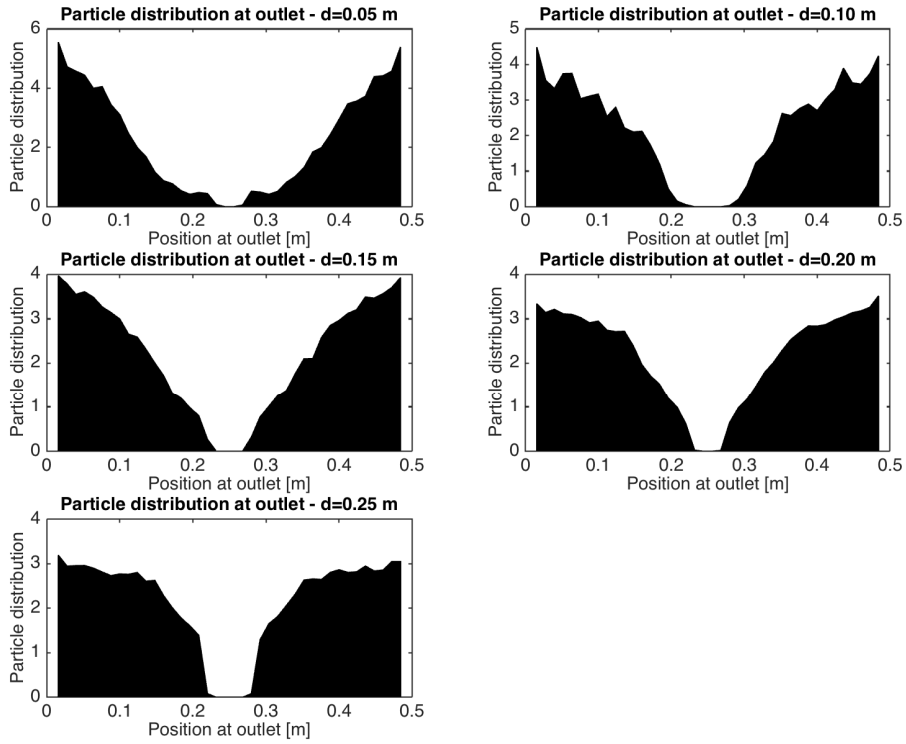

Figure 6.4: The distribution of positions of particles at the outlet, i.e. of particles which the electrostatic precipitator has failed to collect, for the different geometries. The position at the outlet is parametrized by the length from one of the collecting plates. Note that the plate to plate distance is 0.5 m and that the wires are positioned between the plates, which corresponds to the coordinate 0.25 m.

Chapter 7

Conclusions and outlook

In this thesis, we have demonstrated the possibility to split the three-species negative corona discharge problem into a globally one-species and locally three-species problem. This is an efficient approach since it limits the use of the computationally more complex three-species model to a small part of the domain. The approach is validated and applied to analyze a range of geometries that are relevant to automotive spray painting and electrostatic precipitators.

Regarding applications to electrostatic precipitators, we demonstrate how the three-species model can be used to supply boundary conditions when simulating particle collection efficiencies. This is an improvement compared to previous works which e.g. make use of the Kaptzov criterion to set boundary conditions in the parts of the domain where ionization occurs, but which has limited range of validity. Here, we have considered rather idealized parallel plate geometries. On the other hand, more complex geometries can be considered and the benefits of using the three-species model can be expected to be greater as the corona phenomena becomes more directional.

Regarding the application to automotive spray painting, we treated a two-dimensional analog of the ABB G1 rotary spray bell. For this kind of geometry, we obtain a much more directional corona region than for the geometries with electrostatic precipitators. We demonstrate some possibilities to parametrize boundary conditions for the charge density for a one-species model, which could be an efficient way to incorporate results from the three-species model in simulations that optimize the spray painting process.

Finally, we wish to indicate that guided by the results in this thesis, natural next steps could involve:

- To more systematically compare the boundary conditions that are obtained for parallel plate electrostatic precipitators, when using the three-species model instead of the Kaptzov criterion. This could preferably be performed for a geometry with smaller plate to plate distance than those that were considered in this thesis, e.g. the geometry that was used by Farnoosh et al [6]. Obviously, it is also of interest to analyze to which extent the accuracy in the electrostatic boundary conditions affects the particle collection properties.

- To attempt to reproduce and compare results from experimental studies of electrostatic precipitators with those that are obtained by the three-species model.
- To perform a study that analyzes a wider range of electrostatic precipitators. Specifically, focus could be put on geometries with sharp objects that exhibit a high degree of local structure. Such designs are intended to locally enhance the electric field strength which makes the ionization region partial, for which the use of the three-species model is necessary and the solvers that are presented in this thesis are an efficient tool.
- Developing a three dimensional three-species solver. This would make it possible to analyze the ABB G1 rotary spray bell and some more elaborate geometries for electrostatic precipitators. Note that the three-species problem in three dimensions will be very computationally demanding as the size of the meshes increases drastically compared to the two dimensional case at the same time as the model yields matrices with poor sparsity patterns. Due to this, we expect that the use of domain decomposition can play an even more significant role in limiting the computing power that is necessary to solve the problem in three dimensions.

Bibliography

[1] K. Adamiak, P. Atten, *Simulation of Corona Discharge in Point-plane Configuration*, Journal of Electrostatics 61 (2004) 85-98.

[2] K. Adamiak, V. Atrazhev, P. Atten, *Corona Discharge in the Hyperbolic Point-plane Configuration: Direct Ionization Criterion versus Approximate Formulations*, in: IEEE Transactions on Dielectrics and Electrical Insulation 12 (5) (2005) 1025-1033.

[3] K. Adamiak, *Numerical Models in Simulating Wire-plate Electrostatic Precipitators: A Review*, Journal of Electrostatics 71 (2013) 673-680.

[4] W. Egli, U. Kogelschatz, E. A. Gerteisen, R. Gruber, *3D Computation of Corona, Ion Induced Secondary Flows and Particle Motion in Technical ESP Configurations*, Journal of Electrostatics 40&41 (1997) 425-430.

[5] B. Eliasson, U. Kogelschatz, *Basic Data for Modelling of Electrical Discharges in Gases: Oxygen*, Technical Report, Brown Boveri, 1986.

[6] N. Farnoosh, K. Adamiak, G.S.P. Castle, *3-D Numerical Analysis of EHD Turbulent Flow and Mono-disperse Charged Particle Transport and Collection in a Wire-plate ESP*, Journal of Electrostatics 68 (2010) 513-522.

[7] J. Q. Feng, *Application of Galerkin Finite-element Method with Newton Iterations in Computing Steady-state Solutions of Unipolar Charge Currents in Corona Devices*, J. Comp. Phys. 151 (1999) 969-989.

[8] G. E. Georghiou, *Numerical Modelling of Atmospheric Pressure Gas Discharges Leading to Plasma Production*, J. Phys. D: Appl. Phys. 38 (2005) 303–328.

[9] G. W. Hewitt, *The Charging of Small Particles for Electrostatic Precipitation*, AIEE transactions on communication and electronics 76 (3) (1957) 300-306.

[10] T. Johnson, S. Jakobsson, B. Wettervik, B. Andersson, A. Mark, F. Edelvik, *A Finite-volume Method for Electrostatic Three-species Negative Corona Discharge Simulations with Application to Externally Charged Powder Bells*, Journal of Electrostatics 74 (2015) 27-36.

[11] M. Kocik, J. Dekowski, J. Mizeraczyk, *Particle Precipitation Efficiency in an Electrostatic Precipitator*, Journal of Electrostatics 63 (2005) 761–766.

[12] B.P. Leonard, *The Ultimate Conservative Difference Scheme Applied to Unsteady One-dimensional Advection*, Comput. Methods Appl. Mech. Eng. 88 (1991) 17-74.

[13] B.P. Leonard, *Beyond First-order Upwinding: the Ultra-sharp Alternative for Non-oscillatory Steady-state Simulation of Convection*, Int. J. Numer. Methods Eng. 30 (4) (1990) 729-766.

[14] Q. Liu, S. Zhang, J. Chen, *Numerical Analysis of Charged Particle Collection in Wire-plate ESP*, Journal of Electrostatics 74 (2015) 56-65.

[15] A. Mark, R. Rundqvist, F. Edelvik, *Comparison Between Different Immersed Boundary Conditions for Simulation of Complex Fluid Flows*, FDMP 7 (3) (2011) 241-258.

[16] A. Mark, B. G. M. Van Wachem, *Derivation and Validation of a Novel Implicit Second-order Accurate Immersed Boundary Method*, Journal of Computational Physics 227 (2008) 6660-6680.

[17] A. Mark, B. Andersson, S. Tafuri, K. Engström, H. Söröd, F. Edelvik, J. S. Carlson, *Simulation of Electrostatic Rotary Bell Spray Painting in Automotive PAint Shops*, Atomization and sprays 23 (1) (2013) 25-45.

[18] A. M. Meroth, T. Gerber, C. D. Munz, P. L. Levin, A. J. Schwab, *Numerical Solution of Non-stationary Charge Coupled Problems*, Journal of Electrostatics 45 (1999) 177-198.

[19] A. Niewulis, J. Podlin'ski, J. Mizeraczyk, *Electrohydrodynamic Flow Patterns in a Narrow Electrostatic Precipitator with Longitudinal or Transverse Wire Electrode*, Journal of Electrostatics 67 (2009) 123–127.

[20] M. M. Pauthenier, M. Moreau-Hanot, *Charging of Spherical Particles in an Ionizing Field*, Journal de Physique et Le Radium 3 (7) (1932) 590-613.

[21] J. Podlin'ski, *Electrohydrodynamic Gas Flow in a Positive Polarity Wire-plate Electrostatic Precipitator and the Related Dust Particle Collection Efficiency*, Journal of Electrostatics 64 (2006) 259–262.

[22] F. Pontiga, C. Soria, A. Castellanos, *Spatial Distribution of Electrons and Ions in a Negative Corona Discharge*, IEEE 1996 Annual Report of the Conference on Electrical Insulation and Dielectric Phenomena 2 (1996) 671-674.

[23] F. Pontiga, C. Soria b, A. Castellanos, *Electrical and Chemical Model of Negative Corona in Oxygen at Atmospheric Pressure*, Journal of Electrostatics 40&41 (1997) 115-120.

[24] G.G. Raju, *Gaseous Electronics: Theory and Practice*, Taylor and Francis, 2006.

[25] P. Sattari, G. S. P. Castle, K. Adamiak, *FEM–FCT-Based Dynamic Simulation of Corona Discharge in Point–Plane Configuration*, IEEE Transactions on Industry Applications 46 (5) (2010) 1699-1706.

[26] H. J. White, *Particle Charging in Electrostatic Precipation*, AIEE Transactions 70 (1951) 1186-1191.

[27] K. Yanallah, F. Pontiga, Y. Meslem, A. Castellanos, *An Analytical Approach to Wire-to-cylinder Corona Discharge*, Journal of Electrostatics 70 (2012) 374-383.

[28] J. Zhang, K. Adamiak, *A Multi-species DC stationary Model for Negative Corona Discharge in Oxygen; Point-plane Configuration*, Journal of Electrostatics 65 (2007) 459–464.